

**Final results of the EDELWEISS-I dark matter search  
with cryogenic heat-and-ionization Ge detectors**

V. Sanglard,<sup>1,\*</sup> A. Benoit,<sup>2</sup> L. Bergé,<sup>3</sup> J. Blümer,<sup>4,5</sup> A. Broniatowski,<sup>3</sup> B. Censier,<sup>3</sup>  
L. Chabert,<sup>1</sup> M. Chapellier,<sup>6</sup> G. Chardin,<sup>7</sup> P. Charvin,<sup>7,8</sup> S. Collin,<sup>3</sup> M. De Jésus,<sup>1</sup>  
H. Deschamps,<sup>7</sup> P. Di Stefano,<sup>1</sup> Y. Dolgorouky,<sup>3</sup> D. Drain,<sup>1</sup> L. Dumoulin,<sup>3</sup> K. Eitel,<sup>5</sup>  
M. Fesquet,<sup>7</sup> S. Fiorucci,<sup>7</sup> J. Gascon,<sup>1</sup> E. Gerlic,<sup>1</sup> G. Gerbier,<sup>7,8</sup> C. Goldbach,<sup>9</sup>  
M. Goyot,<sup>1</sup> M. Gros,<sup>7</sup> S. Hervé,<sup>7</sup> M. Horn,<sup>5</sup> A. Juillard,<sup>3</sup> M. Karolak,<sup>7</sup> C. Kikuchi,<sup>3</sup>  
A. de Lesquen,<sup>7</sup> M. Luca,<sup>1</sup> J. Mallet,<sup>7</sup> S. Marnieros,<sup>3</sup> L. Mosca,<sup>7</sup> X.-F. Navick,<sup>7</sup>  
G. Nollez,<sup>9</sup> P. Pari,<sup>6</sup> L. Schoeffel,<sup>7</sup> M. Stern,<sup>1</sup> L. Vagneron,<sup>1</sup> and V. Villar<sup>7</sup>

(EDELWEISS Collaboration)

<sup>1</sup>*Institut de Physique Nucléaire de Lyon-UCBL, IN2P3-CNRS,*

*4 rue Enrico Fermi, 69622 Villeurbanne Cedex, France*

<sup>2</sup>*Centre de Recherche sur les Très Basses Températures,*

*SPM-CNRS, BP 166, 38042 Grenoble, France*

<sup>3</sup>*Centre de Spectroscopie Nucléaire et de Spectroscopie de Masse,*

*IN2P3-CNRS, Université Paris XI, bât 108, 91405 Orsay, France*

<sup>4</sup>*Institut für Experimentelle Kernphysik, Universität Karlsruhe (TH),*

*Gaestr. 1, 76128 Karlsruhe, Germany*

<sup>5</sup>*Forschungszentrum Karlsruhe, Institut für Kernphysik,*

*Postfach 3640, 76021 Karlsruhe, Germany*

<sup>6</sup>*CEA, Centre d'Etudes Nucléaires de Saclay,*

*DSM/DRECAM, 91191 Gif-sur-Yvette Cedex, France*

<sup>7</sup>*CEA, Centre d'Etudes Nucléaires de Saclay,*

*DSM/DAPNIA, 91191 Gif-sur-Yvette Cedex, France*

<sup>8</sup>*Laboratoire Souterrain de Modane, CEA-CNRS,*

*90 rue Polset, 73500 Modane, France*

<sup>9</sup>*Institut d'Astrophysique de Paris, INSU-CNRS,*

*98 bis Bd Arago, 75014 Paris, France*

(Dated: September 4, 2018)

## Abstract

The final results of the EDELWEISS-I dark matter search using cryogenic heat-and-ionization Ge detectors are presented. The final data sample corresponds to an increase by a factor five in exposure relative to the previously published results. A recoil energy threshold of 13 keV or better was achieved with three 320 g detectors working simultaneously over four months of stable operation. Limits on the spin-independent cross-section for the scattering of a WIMP on a nucleon are derived from an accumulated fiducial exposure of 62 kg·d.

PACS numbers: 95.35.+d;14.80.Ly;98.80.Es;29.40.Wk

---

\*Email address: [sanglard@ipnl.in2p3.fr](mailto:sanglard@ipnl.in2p3.fr)

## I. INTRODUCTION

The search for the particles constituting the non-baryonic dark matter content of our Universe is a domain of intense experimental activities (see e.g. Ref. [1] for a review). In the so-called direct search [2], one looks for nuclear recoils induced by the scattering on terrestrial targets of Weakly Interacting Massive Particles (WIMPs) that are part of the dark matter halo of our Galaxy. The Minimal SuperSymmetric Model (MSSM), where the WIMP is the neutralino [3] (Lightest Supersymmetric Particle), predicts scattering rates ranging from one interaction per kilogram of detector per week, to less than one interaction per ton per year [4]. The experimental challenge is to discriminate these rare events from the much larger backgrounds from natural radioactivity. The expected recoil energies range typically from a few keV to a few tens of keV, a relatively low energy scale for usual particle physics detectors. Up to now, the best sensitivities have been obtained by cryogenic detectors with nuclear recoil identification capabilities [5, 6, 7, 8, 9]. In these techniques a heat (or phonon) channel measures the energy deposit independently of the nature of the recoiling particle. A second channel measures the ionization yield in a semiconductor crystal (CDMS [5, 6] and EDELWEISS [7, 8]) or the light yield of a scintillating crystal (CRESST [9]). The overwhelming background from  $\gamma$  and  $\beta$  radiation is reduced by factors larger than 1000 by exploiting the fact that electron recoils have larger ionization or scintillation yields than nuclear recoils.

The previous EDELWEISS [8] results were the first to probe the predictions of a first set of supersymmetric models. Since then, CDMS [6] has published new results with a factor four improvement in sensitivity. Limits obtained by the CRESST experiment using W recoils [9] show a sensitivity similar to that of EDELWEISS.

The published results of EDELWEISS were obtained using single 320 g heat-and-ionization Ge detectors, with accumulated fiducial exposures of 5.0 [7] and 13.6 kg·d [8]. Since then the experiment has completed its phase I, reaching its goal to operating simultaneously three detectors in low-background run conditions over a period of several months. In this paper we present the final results of the EDELWEISS-I experiment. A new sample representing a fiducial exposure of 48.4 kg·d is added to the 13.6 kg·d of data presented in Refs. [7, 8]. New limits are established with the total fiducial exposure of 62 kg·d, superseding the previously published results [8]. The origins of the possible backgrounds limiting the sensitivity of the

present setup are discussed. Two key achievements are pursued. The first is to reach an energy threshold better than 20 keV for the detection and discrimination of nuclear recoils. The second is the identification of the nature of possible backgrounds that could appear in the sensitivity domains beyond those first explored in Ref. [8]. In addition to the presentation of the sensitivity reached by the EDELWEISS-I experiment, this work is also an essential preparation for the more ambitious phase II, where up to 120 detectors will be operated in a larger cryostat in an optimized low-radioactivity environment.

## II. EXPERIMENTAL SETUP

The experimental setup is described in detail in Refs. [7, 8, 10]. Only the most relevant aspects as well as the improvements made since then will be summarized in this section.

### A. Shielding

The experiment is located in the Laboratoire Souterrain de Modane (LSM) in the Fréjus tunnel under the French-Italian Alps. The rock coverage, equivalent to 4800 m of water, reduces the cosmic muon flux to 4.5 muons per day for a horizontal detector surface of 1 m<sup>2</sup>. The neutron flux  $\Phi_n$  in the 2-10 MeV range is  $\Phi_n \sim 1.6 \times 10^{-6}$  /cm<sup>2</sup>/s [11, 12]. The detectors are protected from the surrounding  $\gamma$ -ray background with 10 cm of Cu and 15 cm of Pb [13]. Pure nitrogen gas is circulated within this shield to reduce radon accumulation. An additional 7 cm thick internal roman lead shield screens the detectors from radioactive electronic components. The entire setup is protected from the neutron background by an outer 30 cm paraffin shield.

### B. Detectors

Three 320 g cryogenic heat-and-ionization Ge detectors (70 mm in diameter and 20 mm in height with edges beveled at an angle of 45°) are operated simultaneously in a low-background dilution cryostat [13] running at a regulated temperature of  $17.00 \pm 0.01$  mK. They are individually housed in separate 1 mm thick Cu casings, the distance between the Ge surfaces being 13 mm. For the heat measurement, a NTD-Ge thermometric sensor is

glued on each detector. For the ionization measurement, the detectors are equipped with two Al electrodes. One is segmented to define two regions, a central part and a guard ring [10]. The applied collection voltage  $V_{bias}$  is either +6.34 V or -4.0 V.

Over the years, seven detectors have been used. Their characteristics are listed in Table I. For the first three, labeled GeAl6, GeAl9 and GeAl10, the Al electrodes are directly sputtered on the Ge crystal. As shown in Ref. [14], and also observed in Ref. [8], a better charge collection is achieved with a Ge or Si amorphous layer under the electrodes. Therefore, only one of the GeAl detectors was used in a short low-background run [7]. The two detectors with Ge amorphous layers are labeled GGA1 and GGA3, and the two detectors with Si amorphous layers, GSA1 and GSA3.

We present here the results of two new runs in addition to the two low-background runs for which results have been published in Refs. [7, 8]. These two new runs, named 2003i and 2003p (see Sec. II C), have been recorded with a stack comprising the three detectors GSA3, GSA1 and GGA3. The experimental configurations are described in the following.

### C. Data acquisition

The numerical acquisition system is based on a commercial PXI system. For each of the three detectors the measured quantities are two ionization signals from the center and guard electrodes, and one heat signal from the NTD-Ge thermometric sensor. The analog signals are pre-amplified at a cold-FET stage, amplified at ambient temperature, filtered to avoid aliasing and then digitized on two PXI cards. The six ionization channels are recorded with a multiplexed 16-channel PXI-6070E card with 12-bit precision at a sampling rate of 200 ksample/s. The heat signals - for which the time constants are slower by three orders of magnitude relative to the ionization signals - are recorded at a rate of 1 or 2 ksample/s, depending on the data takings, with a slower PXI-6052E card with 16-bit precision.

The data are then transferred via a dedicated 1.5 Gbit/s optical link to the bi-Xeon computer running the acquisition program. To optimize the signal-to-noise ratio, the digitized signal of each channel first passes through a specific IIR (Infinite Impulse Response) numerical bandpass filter tailored to the main features of the noise spectrum. The trigger is defined numerically by requesting that the absolute value of any channel exceeds a given threshold. Up to 2002 and in the first run in 2003 (run 2003i), the trigger was based on the ionization

channels. In the last run in 2003 (run 2003p), it was based on the phonon (or heat) channel. This phonon trigger configuration results in a better sensitivity at low energy.

The ionization trigger setup has already been described in previous publications [7, 8]. It basically scans data blocks in a circular buffer. If the trigger conditions are fulfilled for any ionization channels, the relevant data are saved to disk.

The phonon trigger setup first requires that one of the three heat channels exceeds a pre-defined level. When a trigger is found the relevant ionization information lies in the past, due to its  $\sim 1000$  times faster rise-time. Hence the two corresponding center- and guard-channel buffers are scanned back 20 ms to find the most appropriate signal candidate. This is achieved by performing a convolution of the data with a template of an ionization signal built offline. The maximum of convolution gives the position of the ionization signal. The size of the "search zone" of 20 ms corresponds to the total heat signal rise-time with a safety margin of  $\sim 30\%$ .

When the position of the ionization signal is localized, the relevant portion of data for all channels on each detector is saved to disk, as well as the value of the time difference between the ionization and heat channels computed online. The stored samples correspond to 10 ms of ionization data and 1 s of heat data. In addition, for each event its absolute time of occurrence, the instantaneous temperature of the dilution refrigerator, the results of the online convolution performed by the trigger system, and a bit pattern corresponding to the detectors with a heat signal above the trigger threshold in a 120 ms window are recorded. To avoid triggering twice on the same event, the minimum time between two events is set to 0.76 s, resulting in an equivalent dead time per recorded event.

The data acquisition is automatically stopped for 12 min every 3 hours. This corresponds to the time where the electrodes are short-circuited in order to prevent the accumulation of space charge [15].

#### **D. Signal Processing**

The stored events are re-processed offline. A detailed description of the signal processing can be found in Ref. [10]. In the offline analysis, templates of ionization and heat signals are adjusted with the constraint of the simultaneity of the center, guard and heat signals in a given detector. The piled-up pulses, practically negligible in low-background data, are more

numerous in calibration runs and are taken into account with the simultaneous adjustment of more than one template to each event. The templates are built with a sample of selected 122 keV events from a  $^{57}\text{Co}$  source, one template for each channel and each detector. It was verified that the templates did not vary with time, except at the beginning of the run 2003p when the digital filters have been modified (see Sec. IV C). On Fig. 1(a) and (b) are shown examples of filtered ionization and heat pulses (full lines), respectively, for  $\sim 10$  keV $_{ee}$  signals in the detector GGA3, together with the template fits (dashed lines). These low energy signals are well modelled by the 122 keV pulse template. The  $\chi^2$  of the fits do not depend on the pulse amplitude, showing that the pulse shape does not vary with amplitude, at least up to  $\sim 300$  keV. The cross-talk between the two electrode signals is less than 4 % and remains constant through time. It is treated as described in Ref. [10].

In the phonon trigger data, some events are due to the internal radioactivity of the NTD sensor. For these events, the deposited energy in the NTD is not accompanied by an ionization signal. These so-called NTD events occur at a rate of  $\sim 0.5$  mHz. In this case, the shape of the heat signal is different. To identify these events, each heat sample is processed twice: first with a normal template, and then with the template of a NTD-event pulse. This NTD pulse template is built using a small sample of such events with a large amplitude, detected by the absence of ionization signal and large  $\chi^2$  values for the fit with the normal template. Fig 1(c) shows an example of such NTD pulse (full line) together with the normal template fit (dotted line) and the NTD template fit (dash-dotted line). Most NTD events are rejected, with no loss of efficiency ( $< 0.1$  %) down to a recoil energy of 10 keV, with a test on the ratio of the  $\chi^2$  of the two fits. The remaining NTD events are removed by an offline cut on the ionization energy, included in the determination of the efficiency discussed below.

### III. DETECTOR CALIBRATION

As described in Ref. [10], the heat signal  $E_H$  is calibrated in keV-electron-equivalent (keV $_{ee}$ ). The center and guard electrode signals are also calibrated in keV $_{ee}$  and added to give the total ionization amplitude  $E_I$ . From these two measurements, the recoil energy  $E_R$  and the ionization quenching  $Q$  are deduced event-by-event by correcting for the Joule

heating due to the applied voltage  $V_{bias}$  [16]:

$$E_R = \left(1 + \frac{|V_{bias}|}{\epsilon_\gamma}\right)E_H - \frac{|V_{bias}|}{\epsilon_\gamma}E_I \quad (1)$$

$$Q = \frac{E_I}{E_R} \quad (2)$$

where  $\epsilon_\gamma \cong 3.0$  V for Ge, the applied voltages are  $V_{bias} = +6.34$  V for GeAl6 and  $V_{bias} = -4.0$  V for the GGA and GSA detectors.

The detector calibration follows the method described in Refs. [7, 8, 10]. The calibration of ionization signals at 122 keV is performed using a  $^{57}\text{Co}$  source. It is checked with a  $^{137}\text{Cs}$  source and the X-ray data described later that the ionization channel is linear from 9 to 662 keV. The calibration runs were performed on a monthly basis. Over the entire running period, there is no observable drift in time of the ionization gains. After a first calibration at 122 keV, the heat signal is calibrated by imposing that its ratio to the ionization signal should be unity for all  $\gamma$ -rays. Non-linearities on the heat channel between 0 and 662 keV are determined using  $^{137}\text{Cs}$  data. The dependence in time of the overall heat gain is obtained by monitoring closely the ratio of the ionization and heat signals as a function of time. The largest drifts in heat gain are less than a few percent per hour, and either occur on occasional failure of the temperature regulation system, or within five hours after refilling the cryostat with liquid He. Drifts of up to 10 % in heat gain are corrected as linear functions of time in order to avoid abrupt changes of calibration constants during runs. Data sets with larger drifts are discarded.

Thanks to the improved heat resolution and the increased statistics, it was possible to study in more detail than in the previous work the calibration at very low energy. Summed X-ray peaks are emitted following the electron capture decay of  $^{65}\text{Zn}$  ( $T_{1/2} = 244$  d) and  $^{68}\text{Ge}$  ( $T_{1/2} = 271$  d) due to the activation of the detectors by cosmic rays before their installation at the LSM, and of  $^{71}\text{Ge}$  ( $T_{1/2} = 11.4$  d) activated following  $^{252}\text{Cf}$  neutron source calibrations. These total K-shell energy peaks at 8.98 and 10.37 keV for Zn and Ge decays, respectively, are clearly seen in Fig. 2. They are particularly useful to verify the accuracy of the energy calibration at low energies. For example, using the  $^{57}\text{Co}$  calibration at 122 and 136 keV, the energies of the 8.98 and 10.37 keV X-ray peaks are reproduced within  $0.1 \pm 0.1$  keV.

To select events occurring in the central part of the detector, where the electric field is the



most uniform and the detector better shielded from its environment, a fiducial cut is made by requiring that at least 75 % of the charge signal comes from the center electrode. As measured in Ref. [10], using data recorded with a  $^{252}\text{Cf}$  neutron source, this requirement corresponds to  $55 \pm 1$  % of the total volume for GeAl6 and  $58 \pm 1$  % of the total volume for the GGA and GSA detectors, with slightly different electrode designs. Conservatively, the adopted values are 54 % and 57 %.

Calibrations with a  $^{252}\text{Cf}$  neutron source have been performed for each detector and each run configuration in order to establish the zone in the  $Q$  vs  $E_R$  plane corresponding to a 90 % efficiency to detect nuclear recoils induced by neutron scattering. It has been verified that, in all cases, the nuclear recoil band is well described with the parametrization used previously [7, 8, 17]. Namely, the distribution is Gaussian, centered around  $Q = 0.16E_R^{0.18}$ , and its width  $\sigma_Q$  is given by the propagation of the experimental resolutions on  $E_H$  and  $E_I$  (see Table II), smeared by an additional spread  $C$ , see Eq. 11 from [10]. The constant  $C$  represents the effects of multiple neutron scattering and energy straggling in the stopping of the Ge recoils. The experimental  $\sigma_Q$  in neutron calibrations are well reproduced with  $C=0.035$ . The width of the band for WIMP-induced recoils should not be altered by multiple scattering, but in Ref. [10] it was shown that the band measured in neutron calibration is a conservative estimate of the 90 % efficiency region for WIMP induced recoils.

The same neutron calibrations yield precise measurements of the nuclear recoil detection efficiency as a function of  $E_R$  (and in particular, close to threshold). Here, the large number of neutron-neutron coincidences is used as a source of "minimum bias events". In practice, for a given detector this sample is defined as events where a neutron has been recorded in one of the other two detectors. In previous works [7, 8, 10], samples defined in this way were used to measure the efficiency as a function of the signal used for triggering,  $E_I$ . Here, it is measured as a function of recoil energy  $E_R$ . In order to eliminate NTD events and accept only events with charge amplitude above noise, a 2.5 keV $_{ee}$  cut is applied on the total ionization amplitude of each detector. The trigger efficiency measured after the online phonon trigger and the minimum ionization cut is illustrated for detector GGA3 in Fig. 3. The top panel of this figure shows the  $E_R$  distribution in GGA3 for minimum bias events (dotted histogram), as well as for events where the online trigger has detected a heat signal in GGA3 (dot-dashed histogram), and for events where in addition the ionization signal exceeds 2.5 keV $_{ee}$  (dashed histogram). In coincident data, the time of all ionization signals

is given by the largest amplitude charge signal in any of the detectors. It is thus possible to identify accurately ionization signals that are below  $2.5 \text{ keV}_{ee}$  and to observe (dot-dashed histogram) low-energy events that would be otherwise lost in single detector data. Most of the inefficiency at low energy comes from the  $2.5 \text{ keV}_{ee}$  cut. Fig. 3 also shows the effect of the two additional cuts on  $Q = E_I/E_R$  in the final analysis (full-line histogram): the first one to select neutrons ( $\pm 1.65\sigma$ , corresponding to 90 % efficiency) and the second one to reject  $\gamma$ -rays ( $< -3.29\sigma$ , corresponding to 99.9 % rejection for a Gaussian distribution in  $Q$  centered at one). The truncation at 9 keV is due to the  $\gamma$ -ray rejection cut. The cumulative effect of the trigger and the selection cuts on the efficiency as a function of recoil energy for nuclear recoils is shown in the lower panel of Fig. 3, where this quantity is obtained from the ratio of the full-line and dotted histograms in the top panel. At the plateau, the measured ratio is approximately 80 %. After correcting for neutron coincidences with  $\gamma$ -rays as in for example, inelastic (n,  $\gamma$ ) scattering, it is verified that the defined band contains 90 % of the elastic nuclear recoil interactions.

The "threshold energy" is defined as the energy at which the efficiency reaches half its maximum value. It is a relevant variable for comparing detectors among themselves, and with the detector simulations (see Sec. IV D for details). For GGA3 in the phonon trigger configuration, the energy threshold is  $11 \pm 1 \text{ keV}$  (see Fig. 3). The measured values for the detectors in the different configurations where coincident neutron measurements were possible are listed in Table III. In the run 2003p, the recoil energy thresholds on the three detectors were better than 13 keV. This is better than what is achieved in the run 2003i, where the corresponding values range from 14 to 23 keV. The improvements are due to three factors. Firstly, the baseline heat resolution is generally better than the ionization one (see Table II). Secondly, the ionization signal for nuclear recoils is significantly reduced by the quenching effect. Thirdly, ionization signals with a lower amplitude can be recorded in the phonon trigger configuration because this trigger requires a coincidence between a phonon trigger, with better sensitivity, and an ionization signal greater than  $2.5 \text{ keV}_{ee}$  searched on a short (20 ms) time window immediately preceding the time at which the heat signal is detected.

## IV. DATA SETS

### A. WIMP candidate selection

An event in a detector is considered as a WIMP candidate in the fiducial volume if it obeys the following criteria:

1. More than 75 % of the charge is collected on the central electrode.
2. The ionization signal  $E_I$  exceeds the ionization threshold value (listed in Table III).
3. The  $Q$  and  $E_R$  values are inside the  $\pm 1.65\sigma$  (90 %) nuclear recoil band.
4. The  $Q$  and  $E_R$  values are outside the  $\pm 3.29\sigma$  (99.9 %) electron recoil band.
5. Only this detector participates in the trigger.

For each detector and run configuration, the nuclear and electron recoil bands are calculated using the corresponding experimental resolutions (see Table II). As stated earlier, it was verified that the  $\pm 1.65\sigma$  neutron band contains 90 % of neutron scattering events in  $^{252}\text{Cf}$  calibrations, excluding inelastic events where some energy is deposited by an additional  $\gamma$ -ray. Given the expected statistics in the low-background runs, a safe rejection of  $\gamma$ -rays requires to extend the width of the electron recoil band beyond 2 or  $3\sigma$ , depending on  $E_R$ . Although the  $Q$  distributions in  $\gamma$ -ray calibrations appear to be Gaussian up to  $3\sigma$ , it has not been possible to accumulate enough statistics to verify this assertion with precision. For safety, a width of  $\pm 3.29\sigma$  is adopted, which corresponds to a 99.9 % rejection for a Gaussian distribution. The effective rejection may not be as good, but the procedure yields conservative upper limits on WIMP-nucleon scattering cross-sections (see Sec. VD).

### B. Previous data sets

In 2000 and 2002, two low-background runs have been performed. The results have been published in Refs. [7] and [8], respectively. These data sets have not been reprocessed. However, the nuclear recoil selection has been modified in order to be consistent with the one described above. The only modification relative to Refs. [7, 8] is the removal of the low-energy bound on  $E_R$  that was previously set to either 20 or 30 keV, depending on the energy

for which the efficiency value is approximately constant with energy and close to 90 %. In the present work, this lower bound is replaced by the more natural constraint given by the  $3.29\sigma$   $\gamma$ -ray rejection and the ionization threshold. The reduced efficiency below 20 and 30 keV is taken into account in a later stage of the analysis (see Sec. IV D).

The run 2000 comprises three configurations (see Table III) with ionization thresholds of 5.7, 9.0 and 11.0 keV<sub>ee</sub>. The corresponding fiducial exposures are respectively 3.80, 0.63 and 0.60 kg·d, for a total of 5.03 kg·d. The data are shown in Fig. 2 of Ref. [7]. No nuclear recoil candidates are observed above the analysis threshold of 30 keV used in Ref. [7]. Two events fall within the selection defined in Sec. IV A: at  $(E_R, Q) = (22.5 \text{ keV}, 0.367)$  and  $(25.1 \text{ keV}, 0.312)$ , both recorded in the first configuration. Another event is observed at  $(29.3 \text{ keV}, 0.420)$  in the third configuration. It is excluded by the  $3.29\sigma$   $\gamma$ -ray rejection corresponding to this configuration.

The run 2002 corresponds to a fiducial exposure of 8.6 kg·d with an ionization threshold of 3.5 keV<sub>ee</sub>. As can be seen in Fig. 3 of Ref. [8], five events satisfy the new selection criteria, two of them having recoil energies above 15 keV (18.8 and 119 keV).

### C. New experimental conditions and data sets

For the new runs, the experimental setup was upgraded in order to address the three following points.

- Firstly, the results of the run 2002 [8] together with studies of Ref. [14] suggested that the presence of an amorphous layer under the metallic electrodes improved the charge collection. This was later confirmed with short test runs of detectors with and without an amorphous layer, either in Ge or Si. Consequently, a stack of three detectors with amorphous layers was assembled (GSA3, GSA1 and GGA3) for an extended low-background run.
- Secondly, the runs 2000 and 2002 had been limited by cryogenic problems caused indirectly by the regular disruptions associated with the manual procedure for the filling of cryogenic fluids. It was therefore decided to install an automatic liquid He filling system with an associated monitoring system.

- Finally, it had been noticed that the baseline noise levels on the ionization and heat channels were very sensitive to the quality of the electrical connections between the detectors, the cold FETs and the warm amplifiers. For the new low-background runs, the wiring was re-designed for an improved reliability.

The new data sets are separated into two running periods.

In the first one (run 2003i) the automatic filling system was being commissioned. For safety reasons, the automatic monitoring of the liquid He level was permanently on, at the expense of additional noise on the signals. Despite the improvements in wiring, large fluctuations in baseline noise were still observed on the GSA1 heat channel, sometimes reaching levels at which the induced cross-talk observed in the other detectors degraded significantly their resolutions. As shown later, this is particularly true just after He refilling, indicating a high sensitivity to microphonic noise.

The second running period (run 2003p) corresponds to a new stable configuration, where the problems associated with noise due to the He monitoring system and other sources of microphonics were cured. As the He filling system had proved its reliability, the monitoring was switched off during the low-background runs. The sensitivity to the microphonic noise was reduced when the stray capacitance between the cold FETs and the warm amplifiers was decreased by replacing a patch panel interface between them with soldered connections. These improvements were performed and tested in a few weeks, while keeping the three detectors at millikelvin temperatures. Before resuming the low-background run, the ionization trigger was replaced by the phonon trigger, after a thorough comparison of their relative performances. At the same time, the online numerical filters on the center electrode signals were adjusted to the new noise spectra, resulting in improved baseline resolutions.

As a result, the varying quality of the data recorded in the run 2003i required some selection, described in the following, while less than 0.5 % of the data of the run 2003p (3.5 out of the 1140 hours) had to be excluded because of data quality cuts. In order to avoid biases, the data quality cuts are not made event-by-event. Instead, the data quality is evaluated on an hourly basis.

If one of the two following criteria fails, the entire hour is rejected and deducted from the total exposure.

- The first criterion is devised to reject periods where the baseline noise of the heat channels reaches levels at which it reduces significantly the nuclear recoil acceptance at low energy, for example if the  $3.29\sigma$   $\gamma$ -ray rejection removes events with  $E_R > 30$  keV. In addition, this cut removes effectively periods where this noise changes rapidly and the baseline resolution (and therefore the width of the nuclear and electron recoil bands) cannot be evaluated reliably. The FWHM baseline resolutions of the heat channel of the three detectors are shown as a function of time in Fig. 4 and 5 for the runs 2003i and 2003p, respectively.

The baseline resolution of a given detector is calculated from the dispersion of amplitudes of events where this detector did not participate in the trigger. It is evaluated for every hour, with a three-hour averaging window. The dotted lines in Fig. 4 represent times when the cryostat was re-filled with liquid He. This procedure induces microphonic perturbations that persist for hours, explaining most of the observed short episodes of degradation of the baseline. These periods are removed by eliminating all hours during which the average baseline deviates significantly from its typical value. The cuts are set at 2.5, 5.0 and 1.0 keV<sub>ee</sub> for GSA3, GSA1 and GGA3, respectively. The detector GSA1 in the run 2003i was particularly sensitive to microphonics. After 900 hours of low-background data taking, the heat channel started to oscillate and it contaminated its ionization channel and had to be removed from the trigger. Its read-out electronics was switched off a few days later when it was established that it also deteriorated the noise conditions of GSA3. In the selected periods for GSA1, there are still important fluctuations of the hourly average of the heat FWHM. In order to evaluate more accurately the width of the nuclear recoil band for this sample, the GSA1 data are divided into two subsets, according to whether the average resolution is below or above 3 keV<sub>ee</sub> (named Quality 1 and Quality 2 respectively). Consequently, two subsets and two values of heat baseline FWHM appear in Table II for GSA1 in the run 2003i. The FWHM cut effect on the data sets is the following: out of the 1700 hours of the run 2003i, this cut removes 3.7 %, 51.7 % and 0.2 % of the data set for GSA3, GSA1 and GGA3, respectively, while no data are removed from the run 2003p.

- The second criterion is that the drift in heat gain be less than 10 %, as discussed in the previous section. In the run 2003i, this cut removes 0.8 % of the data for GGA3 and nothing for the other two detectors. In the run 2003p, only one episode of 3.5 hours is rejected out of 1140 hours of low-background run due to a failure of the temperature regulation resulting in a drift exceeding 1 mK.

To calculate the exposure in kg·days, the accepted hours are multiplied by the fiducial masses. The calculation also takes into account the 6 % loss due to regular shorting of the electrodes and the dead-time losses. The fraction of dead time is 4 % in run 2003p, and varies from 8 % to 10 % in the run 2003i, depending on the detector.

In total, the fiducial volume data of the runs 2003i and 2003p represent 25.7 and 22.7 kg·d, respectively. The data quality in the run 2003p is more uniform, as the nuclear recoil bands of the three detectors have very similar widths in this configuration. The three detectors remained extremely stable over the entire four-month period that covered the run 2003p and the long calibration runs.

#### D. Simulation of WIMP detection efficiency

In order to derive limits on the spin-independent scattering rate of WIMPs in the detectors from the observed distribution of events as a function of energy, it is necessary to take into account the experimental efficiency. The experimental thresholds on ionization energy and the resolution of the heat and ionization measurements are inputs of a Monte Carlo simulation of the detector response to WIMPs of given masses between 10 GeV/c<sup>2</sup> and 5 TeV/c<sup>2</sup>.

The starting point of the simulation is with the analytical calculation of the recoil energy spectrum using the formula and the prescriptions of Ref. [2]. A spherical isothermal halo of WIMPs with a local density of 0.3 GeV/c<sup>2</sup>/cm<sup>3</sup> is assumed, with a *rms* velocity of 270 km/s, an escape velocity of 650 km/s and an Earth-halo relative velocity of 235 km/s. The spectrum is multiplied by the form factor for coherent scattering proposed in Refs. [2, 18].

This analytical recoil energy spectrum is then convolved with the experimental resolutions. To do this, recoil events are simulated with recoil energy values  $E_R$  randomly distributed according to the analytical calculation. The value of the quenching factor  $Q$  is randomly chosen in a Gaussian distribution centered at  $Q = 0.16E_R^{0.18}$  with a *rms* value  $C = 0.035$

(see Sec. III).  $E_R$  and  $Q$  are converted into ionization and heat signals using the inverse of Eqs. 1 and 2. The ionization and heat signals are then independently smeared using the measured resolutions at 0 and 122 keV listed in Table II, interpolated using the method of Ref. [10].

The smeared values for the recoil energy  $E_R^*$  and quenching factor  $Q^*$  are calculated from the smeared ionization and heat signals  $E_I^*$  and  $E_H^*$  using Eqs. 1 and 2. The simulated data are then subjected to the same cuts as the physics data, namely: the cut on the ionization energy, the  $1.65\sigma$  selection of nuclear recoils and the  $3.29\sigma$  rejection of electron recoils.

These calculations are repeated for the eleven configurations listed in Table III, normalized to the corresponding exposure and summed. The result is a predicted energy spectrum for each WIMP mass for the entire EDELWEISS-I data set. The limits on the WIMP-nucleon scattering cross-section as a function of WIMP mass are obtained by comparing directly these predicted spectra to the data (see Sec. V D).

To check the validity of the simulation, an efficiency as a function of recoil energy is calculated by dividing the predicted spectrum by the result of the analytical calculation. For a given run configuration, this curve can be compared to the results of the efficiency measurement performed with neutron coincidences. In Table III are compared the simulated and measured energies at which half of the maximal trigger efficiency is reached. The simulation agrees with the measured values to within 1 keV. No measurement is available for GeAl6 because of the absence of neutron coincidence data. For GSA1, there is only one measurement because the neutron calibration was done when the heat baseline resolution was  $2.4 \text{ keV}_{ee}$ , corresponding to the "Quality 1" configuration (see Sec. IV C).

The simulated efficiencies as a function of recoil energy for the entire EDELWEISS-I data set, and also separately for the runs 2000+2002, 2003i and 2003p are shown in Fig. 6, for a WIMP mass of  $100 \text{ GeV}/c^2$ .

The significant increase in efficiency at low energy obtained with the phonon trigger configuration is clearly displayed. For the entire data set, the efficiency reaches half of its maximal value at 15 keV, and 75 % at 20 keV.



## V. RESULTS AND DISCUSSION

### A. Experimental results

For the run 2003p, the event rate in the total volume of the three detectors before the nuclear recoil selection and  $\gamma$ -ray rejection is  $2.00 \pm 0.03$  evt/keV/kg/d between 30 and 100 keV. The fiducial volume selection reduces the raw rate to  $1.31 \pm 0.03$  evt/keV/kg/d in the same energy range. A significant fraction of these events are coincidences between detectors: the single rate is  $0.98 \pm 0.03$  evt/keV/kg/d. Most of these events are electron recoils as can be seen in Figs. 7 to 10 showing the distributions of  $Q$  as a function of  $E_R$  for the runs 2003i and 2003p. The corresponding figures for the runs 2000 and 2002 can be found in Refs. [7] and [8], respectively.

In total, EDELWEISS-I has accumulated 62 kg·d of fiducial volume data. The recoil energy spectrum of all the events passing the nuclear recoil selection described in Sec. IV A is shown in Fig. 11.

Most counts are below 30 keV (53 counts), only three are between 30 and 100 keV, and three more are between 100 and 200 keV. The average count rate between 30 and 200 keV is  $6 \times 10^{-4}$  counts/keV/kg/d. Sixteen counts are observed between 20 and 30 keV, and eighteen more between 15 and 20 keV. The few counts observed below 15 keV must be interpreted with care, as the efficiency drops rapidly in this region. This drop explains the low-energy shape of the simulated WIMP spectra shown on the same figure, calculated for different WIMP masses and an arbitrary choice of the spin-independent WIMP-nucleon scattering cross-section  $\sigma_{W-n} = 10^{-5}$  pb. Indeed, as it will be shown later, the range below 15 keV is not used for setting limits on  $\sigma_{W-n}$ .

### B. Compatibility between the different data sets.

To check whether the 2000+2002, 2003i and 2003p data sets are compatible and can be added, the following test has been performed. First, the total spectrum of Fig. 11 has been corrected for the total efficiency for the 62 kg·d, as calculated by the simulation and shown in Fig. 6.

Then, in Fig. 12, this corrected spectrum is alternatively multiplied by the simulated efficiencies of the runs 2000+2002, 2003i and 2003p and compared with the corresponding data

set. As no significant deviations from the average behavior are observed above 15 keV, it is justified to add the three data sets together. The factor four increase in exposure and the significant increase in efficiency at low energy explains why 16 events are observed between 20 and 30 keV in the new data set while none were reported in Refs. [7, 8]. Conversely, the few events observed just below the 20 and 30 keV analysis thresholds in Refs. [7, 8] are consistent with the expectations deduced from the new data set recorded with a much better efficiency at low energy.

### C. Data interpretation

In the following section, the experimental spectrum of Fig. 11 will be interpreted in terms of a 90 % C.L. limit on the WIMP scattering rate without subtracting any background. However, it is clear from the comparison with the simulated WIMP spectra that no single WIMP mass can explain the entire spectrum. This suggests that part of the spectrum may be attributed to non-WIMP background. As it will be shown in this section, this conclusion can also be reached independently by studying the behavior of the data lying just above the nuclear recoil band, and by studying coincidences between the detectors.

Fig. 13 shows the distributions of the normalized quenching

$$D = \frac{Q - Q_n(E_R)}{1 - Q_n(E_R)} \quad (3)$$

for the data recorded by the three detectors in the run 2003p, for three intervals of recoil energy.

With this variable, where  $Q_n(E_R) = 0.16E_R^{0.18}$ , nuclear and electron recoils should appear as peaks centered at 0 and 1, respectively, independent of  $E_R$ . Indeed, the superposed hatched histograms represent the distributions recorded in neutron and  $\gamma$ -ray calibrations. The  $\gamma$ -ray calibration data are normalized to have the same number of counts above  $D = 1$  as in the low-background run. This clearly shows that the latter distribution is not symmetric around  $D = 1$  as it is in  $\gamma$ -ray calibrations. In the low-background run, the tail extends down to  $D = 0$ , especially at low recoil energy. Below  $E_R = 40$  keV, the tail reaches down to the region where neutrons and WIMPs are expected. This is close to the energy below which the event rate in the nuclear recoil band increases rapidly (see Fig. 11). This type of tail in  $D$  (and thus in  $Q$ ) is generally attributed to bad charge collection of electron recoils near

the surface of the detector [14].

As seen in Fig. 14, this tail is significantly reduced when requiring a coincidence between detectors. This suggests that the mean free path of the radiation at the origin of the events in the tail is less than the 2 mm of Cu that separates two neighboring detectors. However, the precise shape of the tail is not known and is difficult to predict, especially near the nuclear recoil band. Therefore, no attempts have been made to subtract a background contribution from this source to the observed rate in the nuclear recoil band.

The study of coincidences between the detectors in the low-background run gives a robust evidence for another possible source of background: a residual neutron flux. One coincident event between two nuclear recoils is observed between the fiducial volume of GGA3 ( $E_R = 15$  keV,  $Q = 0.27$ ) and the outer volume in the neighboring detector GSA1 ( $E_R = 14$  keV,  $Q = 0.28$ ). In Ref. [5], is presented the case where two apparent nuclear recoils in neighboring detectors are due to the coincidence of two surface electrons with both charge collections being at the lower end of the tail in  $Q$ . This process is unlikely in the EDELWEISS-I geometry, where the 2 mm of Cu separating the detectors should prevent a single electron or an electron cascade to touch two detectors. Indeed, Fig. 14 clearly demonstrates that the coincident events are mainly associated with good charge collection down to low recoil energy, and, conversely, bad charge collections are associated with single events. The observed coincidence is very likely due to two coincident neutron interactions. Monte Carlo simulations of the neutron background based on the measured neutron flux at the LSM tend to predict single event rates of the order of 1 event per 62 kg·day, but the uncertainty on the absolute scale is large. The simulations also predict that the ratio of singles to coincidences for neutron scatters is approximately 10 to 1, for neutrons from the rock radioactivity. This is also the ratio measured in neutron calibrations with a  $^{252}\text{Cf}$  source. It is thus possible that some of the events in Fig. 11 are due to a residual neutron background. On the other hand, given a rate of one neutron per 62 kg·day and a probability for this event to be a coincidence of the order of 10 %, it is also possible that none of the single events are neutrons.

A close inspection of the right panel of Fig. 10 suggests a third possible source of background. There is an accumulation of events along the hyperbola corresponding to the ionization threshold of  $2.5 \text{ keV}_{ee}$ . This may indicate that the cuts (see Sec. IID) do not remove all NTD-events. However the recoil energy of most of these events appearing in the nuclear

recoil band is below 15 keV and they do not affect significantly the derived WIMP exclusion limits for WIMP masses above 25 GeV/ $c^2$  (see Sec. VD).

In summary, studies based on independent data sets confirm that two sources of background may contribute significantly to the observed rate in the nuclear recoil band: surface electrons and neutrons. In the absence of more detailed studies, it is not possible to conclude quantitatively and therefore no background subtraction is performed for the estimate of the limits on the WIMP collision rate in the detectors.

#### D. Neutralino scattering cross-section limits

In order to set upper limits on the cross-section of the spin-independent scattering of a WIMP on a nucleon  $\sigma_{W-n}$  as a function of the WIMP mass  $M_W$ , the optimum interval method of Ref. [19] is used. This method is well adapted to the present case, where no reliable models are available to describe potential background sources and no subtraction is possible. This method can be summarized in the following way: for each mass  $M_W$ , the upper limit on  $\sigma_{W-n}(M_W)$  is calculated using the number of events observed in the recoil energy interval that provides the strongest constraint. Of course, the 90 % C.L. limits on  $\sigma_{W-n}(M_W)$  that would be derived from these carefully chosen intervals by using simple Poisson statistics would be biased and too optimistic. Using Monte Carlo simulations, these biases have been precisely tabulated in [19] in such a way that they can be corrected for and thus derive reliable 90 % C.L. limits. This method automatically determines which energy interval provides the strongest constraint on the presence of a signal. This energy interval may contain events. No background is subtracted, and indeed in the presence of a background having the same energy spectrum as the WIMP signal, the derived 90 % C.L. limit is similar to the Poisson limit based on the total number of observed events in the entire interval.

The inputs of the method are *i*) the individual recoil energies of the nuclear recoil candidates (see Fig. 11) and *ii*) the expected recoil energy spectra for WIMPs, calculated using the simulation described in Sec. IV D, as a function of WIMP mass. We use  $E_R > 15$  keV, corresponding to the recoil energy where the efficiency reaches half of its maximal value. The resulting 90 % C.L. limits on  $\sigma_{W-n}(M_W)$  are shown in Fig. 15.

As this method determines the energy interval that constrains the most the signal, this in-

formation provides some assistance in the interpretation of the observed spectrum.

The lower and upper bounds of the selected energy intervals are shown in Fig. 16, together with the number of events in the corresponding intervals. For  $M_W > 25 \text{ GeV}/c^2$ , the selected intervals are in the energy range from 28.4 to 86.6 keV. This corresponds well to what is observed in Fig. 11, where the experimental spectrum is compared with the expected signal for WIMPs of different masses and an arbitrary choice of  $\sigma_{W-n} = 10^{-5} \text{ pb}$ . Most of the observed events are below  $E_R = 30 \text{ keV}$ . In contrast, for  $M_W > 20 \text{ GeV}/c^2$ , a significant part of the recoil spectra lies above this energy. For masses in the 20 - 25  $\text{GeV}/c^2$  range, the spectrum is strongly peaked below 30 keV, and the experimental data provide a much weaker constraint on  $\sigma_{W-n}$ . For this WIMP mass interval, the best limits are obtained from the 30 events in the energy range from 15.9 to 51.1 keV and are similar to the corresponding Poisson limits.

When comparing the limits shown in Fig. 15 with theoretical predictions, one should take into account the large theoretical uncertainties associated with the astrophysical and nuclear model parameters. These were chosen according to the prescriptions of Ref. [2] that provide a framework for comparing the sensitivities of the different experiments. The experimental systematic uncertainties on the present limits that are relevant for this kind of comparison have been studied. Since the results rely heavily on the recoil energy interval between 28.4 and 86.6 keV, the uncertainties on the energy threshold ( $\pm 1 \text{ keV}$ , see Table III) and on the NTD event cut ( $< 0.1 \%$  down to 10 keV, Sec. IID) have a negligible influence. More important are the contribution from the determination of the fiducial volume and of the position and width of the nuclear recoil band. These effects are discussed in Ref. [10]. Here, they both correspond to  $\sim 2 \%$  uncertainties on the experimental efficiency in the relevant energy range, although these may be overestimations since conservative choices are made in the experimental determination of these quantities [10]. In addition, the 1 % uncertainties on the absolute ionization and heat calibration at low energy (0.1  $\text{keV}_{ee}$  at 10  $\text{keV}_{ee}$ ) correspond to  $\sim 2 \%$  uncertainty on the efficiency in the 28.4 - 86.6 keV range. The quadratic sum of these uncertainties is 4 %. This attests the simplicity and robustness of the data analysis of the EDELWEISS heat-and-ionization detectors.

A common systematic uncertainty to all bolometric experiments is the determination of the quenching factor of the heat or phonon signal. Present direct [20] and indirect [21] measurements are compatible with unity at the  $\sim 10 \%$  level. If taken as an uncertainty, this

range correspond to a  $\sim 10\%$  variation of the limit for  $M_W = 100 \text{ GeV}/c^2$ , increasing up to  $\sim 20\%$  at  $50 \text{ GeV}/c^2$ .

The present limits are very similar to our previously published results (see Fig. 15). These limits can also be expressed simply in terms of rate of nuclear recoils between 30 and 100 keV, a range over which the detector efficiency is approximately constant and equal to 90 % in all configurations (see Fig. 6). In 2000-2002, no events were observed in a fiducial exposure of 13.6 kg·d. Taking into account the 90 % efficiency for nuclear recoil over this energy range, this corresponds to an effective exposure of 12.2 kg·d). It results in a 90 % C.L. limit of 0.19 events/kg/day for nuclear recoils between 30 and 100 keV. A similar rate limit is derived from the 2003 data set alone: the 3 events observed between 30 and 100 keV in the effective exposure of 43.5 kg·d correspond to a limit of 0.15 events/kg/d at 90 % C.L.. For the combined data set, the effective exposure is 55.8 kg·d and the limit at 90 % C.L. is 0.12 events/kg/d between 30 and 100 keV.

In Fig. 15, the present limits are compared with other experiments (CDMS [5, 6] and CRESST [9]). Because of the observed events, the EDELWEISS-I limits are a factor 3 to 4 higher than the limits given by CDMS-II, where surface events are efficiently rejected by phonon timing cuts [6].

## VI. CONCLUSION

The EDELWEISS collaboration has searched for nuclear recoils due to the scattering of WIMP dark matter using several 320 g heat-and-ionization Ge detectors operated in a low-background environment in the Laboratoire Souterrain de Modane. Up to three detectors have been operated simultaneously, with consistent results. In the final EDELWEISS-I setup, stable running conditions were achieved over periods of four months with a recoil energy threshold better than 13 keV on the three detectors. In the total fiducial exposure of 62 kg·d, 40 nuclear recoil candidates are recorded between 15 and 200 keV. Three of them are between 30 and 100 keV, a critical energy range for establishing limits on WIMP interactions in the present experiment. The study of detector coincidences and of the charge collection reveals the presence of two likely sources of background: a residual neutron background and surface electron-recoil events. Nevertheless, the limits obtained on spin-independent WIMP-nucleon scattering cross-section are very similar to the previously published results based

on the initial 13.6 kg-d exposure [8]. The present results supersede those of Refs. [7, 8]. The successful operation of the EDELWEISS-I setup has provided important information for the preparation of the EDELWEISS-II phase. The experimental volume in the EDELWEISS-I setup was limited to one liter. In the new setup under construction, the larger size dilution cryostat (50  $\ell$ ) will be able to house up to 120 detectors, increasing the rate at which exposure can be accumulated. The large number of detectors (28 in a first stage) and the corresponding increase in coincidence rate should facilitate the diagnostic regarding the actual level of the residual neutron flux. This flux should also be drastically reduced by the installation of a 50 cm polyethylene shielding offering a more uniform coverage over all solid angles. In addition, a scintillating muon veto surrounding the experiment should tag neutrons created by muon interactions in the shielding. Regarding the surface electron background, more care is taken in the selection of all materials surrounding the detectors. The collaboration is also developing new detectors with NbSi athermal phonon sensors that can tag surface events [23].

### **Acknowledgments**

The help of the technical staff of the Laboratoire Souterrain de Modane and the participant laboratories is gratefully acknowledged. This work has been partially supported by the EEC Applied Cryodetector network (Contracts ERBFMRXCT980167, HPRN-CT-2002-00322) and the ILIAS integrating activity (Contract RII3-CT-2003-506222)

- 
- [1] A. Morales, Nucl. Phys. B (Proc. Suppl.) **114**, 39 (2003).
- [2] J.D. Lewin and P.F. Smith, Astropart. Phys. **6**, 87 (1996).
- [3] G. Jungman, M. Kamionkowski, and K. Griest, Phys. Rep. **267**, 195 (1996); G. Bertone, D. Hooper and J. Silk, Phys. Rep. **405**, 279 (2005).
- [4] J. Ellis, A. Ferstl, K. A. Olive, and Y. Santoso, Phys. Rev. D **67**, 123502 (2003); E. A. Baltz and P. Gondolo, Phys. Rev. D **67**, 063503 (2003); A. Bottino, F. Donato, N. Fornengo, and S. Scopel, Phys. Rev. D **63**, 125003 (2001); Y. G. Kim, T. Nihei, L. Roskowski, and R. Ruiz de Austri, J. High Energy Phys. **12**, 034 (2002); G. Belanger *et al.*, Nucl. Phys. B **706**, 411 (2005).
- [5] D.S. Akerib *et al.*, Phys. Rev. D **68**, 082002 (2003); D. Abrams *et al.*, Phys. Rev. D **66**, 122003 (2002).
- [6] D.S. Akerib *et al.*, Phys. Rev. Lett. **93**, 211301 (2004).
- [7] A. Benoit *et al.*, Phys. Lett. B **513**, 15 (2001).
- [8] A. Benoit *et al.*, Phys. Lett. B **545**, 43 (2002).
- [9] Angloher *et al.*, Astropart. Phys. (to be published), astro-ph/0408006.
- [10] O. Martineau *et al.*, Nucl. Instrum. Methods Phys. Res. A **530**, 426 (2004).
- [11] V. Chazal *et al.*, Astropart. Phys. **9**, 163 (1998).
- [12] G. Chardin and G. Gerbier, in *Proceedings of the 4th International Workshop on Identification of Dark Matter*, edited by N.J.C. Spooner and V. Kudryavstev (World Scientific, Singapore, 2003) pp. 470-476.
- [13] A. de Bellefon *et al.*, Astropart. Phys. **6**, 35 (1996).
- [14] P.N. Luke, C.P. Cork, N.W. Madden, C.S. Rossington, and M.F. Wesela, IEEE Trans. Nucl. Sci. **39**, 590 (1992); P.N. Luke, C.S. Rossington, and M.F. Wesela, IEEE Trans. Nucl. Sci. **41**, 1074 (1994); T. Shutt *et al.*, Nucl. Instrum. Methods Phys. Res. A **444**, 340 (2000); T. Shutt *et al.*, in *Low Temperature Detectors*, edited by F.S. Porter, D. McCammon, M. Galeazzi, and Stahle, AIP Conf. Proc. No. 605 (AIP, Melville, NY, 2002) pp. 513-516.
- [15] B. Censier *et al.*, Nucl. Instrum. Methods Phys. Res. A **520**, 156 (2004).
- [16] B. Neganov and V. Trofimov, Otkrytia i Izobreteniya **146**, 215 (1985); P.N. Luke, J. Appl. Phys. **64** 6858 (1988); M. Chapellier *et al.*, Physica B **284-288**, 2135 (2000).



- [17] P. Di Stefano *et al.*, *Astropart. Phys.* **14**, 329 (2001).
- [18] R.H. Helm, *Phys. Rev.* **104**, 1466 (1956); J. Engel, *Phys. Lett. B* **264**, 114 (1991); G. Fricke *et al.*, *Atomic Data and Nuclear Data Tables* **60**, 177 (1995).
- [19] S. Yellin, *Phys. Rev. D* **66**, 032005 (2002).
- [20] E. Simon *et al.*, *Nucl. Instrum. Methods Phys. Res. A* **507**, 643 (2003); A. Alessandrello *et al.*, *Phys. Lett. B* **408**, 465 (1997); A. Alessandrello *et al.*, *Phys. Lett. B* **384**, 316 (1996); J. W. Zhou *et al.*, *Nucl. Instrum. Methods Phys. Res. A* **349**, 225 (1994).
- [21] T. Shutt *et al.*, *Phys. Rev. Lett.* **69**, 3425 (1992).
- [22] R. Bernabei *et al.*, *Phys. Lett. B* **480**, 23 (2000).
- [23] S. Marnieros *et al.*, *Nucl. Instrum. Methods Phys. Res. A* **520**, 185 (2004).

TABLE I: Main parameters of the detectors used in EDELWEISS-I, i(p) denotes ionization (phonon) trigger conditions (see Sec. II C).

Run	Detector	Mass (g)	Amorphous layer		Al electrode thickness (nm)	$T_{running}$ (mK)	$V_{bias}$ (V)
			Material	Thickness (nm)			
2000	GeAl6	321.6	none		100	27	+6.34
2002	GGA1	318.5	Ge	60	70	17	-4
2003i	GSA3	297.0	Si	25	64	17	-4
and	GSA1	313.7	Si	50	70	17	-4
2003p	GGA3	324.4	Ge	50	100	17	-4

TABLE II: Full-width at half-maximum (FWHM) resolutions (in  $\text{keV}_{ee}$ ) for heat and ionization signals obtained for the detectors used in EDELWEISS-I, typical errors are less than  $\sim 10\%$ .

Run	Detector	Baseline resolution ( $\text{keV}_{ee}$ )			Resolution at 122 $\text{keV}_{ee}$ ( $\text{keV}_{ee}$ )		
		Ionization		Heat	Ionization		Heat
		Center	Guard	Total			
2000	GeAl6	2.0	1.4	2.4	2.2	2.8	3.5
2002	GGA1	1.3	1.3	1.8	1.3	2.8	3.5
	GSA3	1.1	1.2	1.6	1.6	2.1	3.0
2003i	GSA1 <sup>a</sup>	1.4	1.1	1.8	2.4	2.6	4.0
	GSA1 <sup>b</sup>	1.4	1.5	2.1	4.6	2.8	5.0
	GGA3	1.7	2.0	2.6	0.44	3.5	3.2
	GSA3	1.1	1.4	1.8	1.7	2.4	3.0
2003p	GSA1	1.2	1.4	1.8	0.80	2.8	1.4
	GGA3	1.1	1.6	1.9	0.40	3.1	2.5

<sup>a</sup>Quality 1 data (see Sec. IV C for explanation).

<sup>b</sup>Quality 2 data (see Sec. IV C for explanation).

TABLE III: Thresholds for EDELWEISS-I low-background run data sets. The quoted thresholds correspond to the energy at which the efficiency for nuclear recoils reaches half its maximum value of 90 %. The ionization and heat thresholds are measured at trigger level (see Sec. III), with uncertainties less than  $\pm 0.5 \text{ keV}_{ee}$ ; the recoil energy thresholds are measured after all analysis cuts, with a  $\pm 1 \text{ keV}$  uncertainty. The simulated recoil energy thresholds are obtained for  $M_W = 100 \text{ GeV}/c^2$  (see Sec. IV D) with uncertainties less than  $\pm 1 \text{ keV}$ .

Run	Detector	Ionization threshold ( $\text{keV}_{ee}$ )	Heat threshold ( $\text{keV}_{ee}$ )	Measured recoil energy threshold (keV)	Simulated recoil energy threshold (keV)	Fiducial volume exposure (kg·d)
2000	GeAl6	5.7			23	3.80
		9.0			31	0.63
		11.0			37	0.60
2002	GGA1	3.5		14	14	8.6
	GSA3	3.3		14	13	9.16
2003i	GSA1 <sup>a</sup>	4.6		18	18	2.37
		4.6			24	2.81
		5.8		23	21	11.31
	GSA3	2.5	4.3	13	12	7.20
2003p	GSA1	2.5	2.3	12	11	7.60
		2.5	1.6	11	11	7.86

<sup>a</sup>Quality 1 data (see Sec. IV C for explanation).

<sup>b</sup>Quality 2 data (see Sec. IV C for explanation).

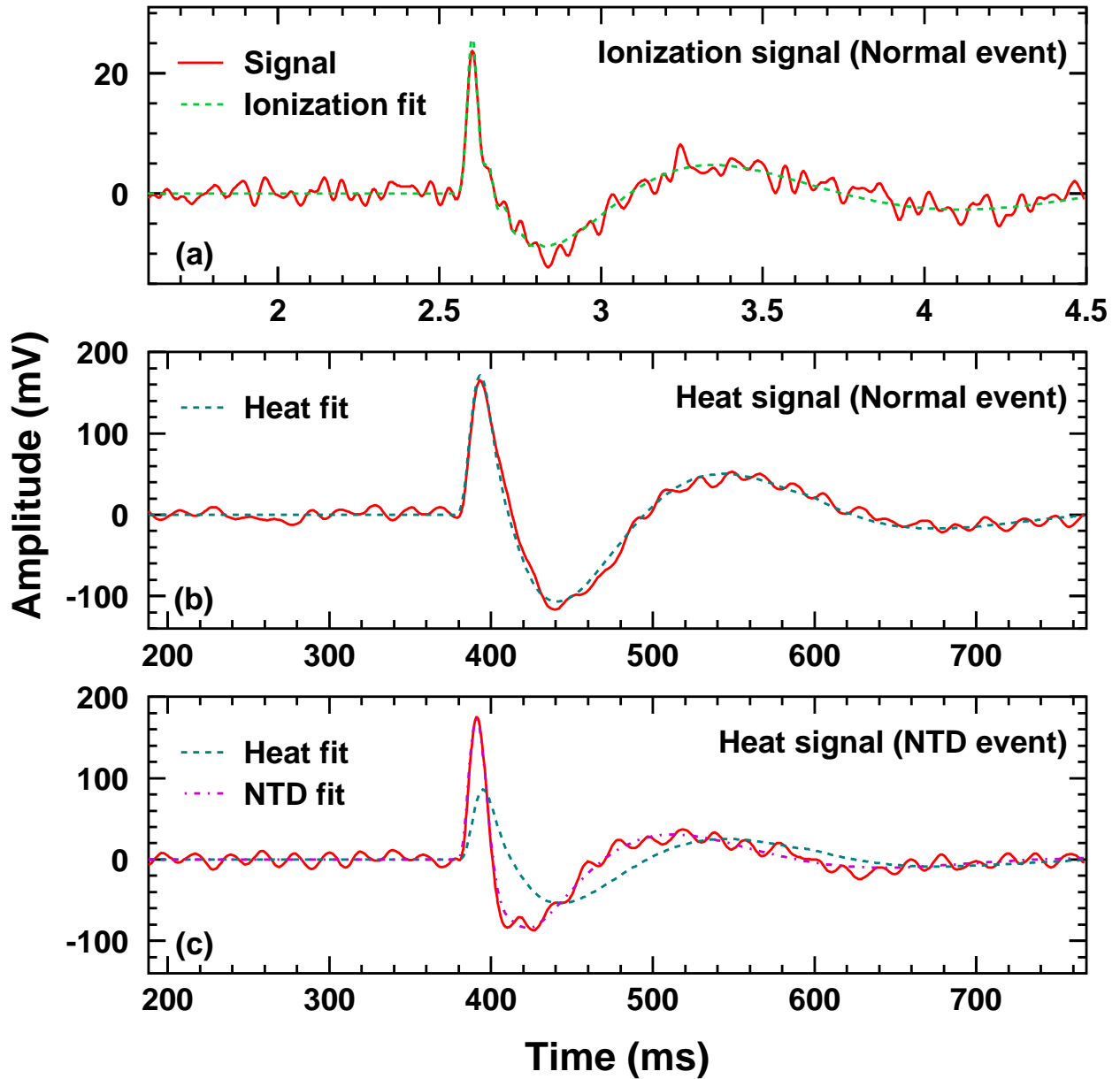


FIG. 1: Example of filtered heat and ionization pulses for  $\sim 10$  keV $_{ee}$  signals (full lines) together with the template fit (dashed lines) for an ionization (center electrode) signal (a) and for the corresponding heat signal (b). In (c) is shown an example of a NTD event (see text) together with the template fits for a normal heat signal (dashed line) and for a NTD signal (dash-dotted line)

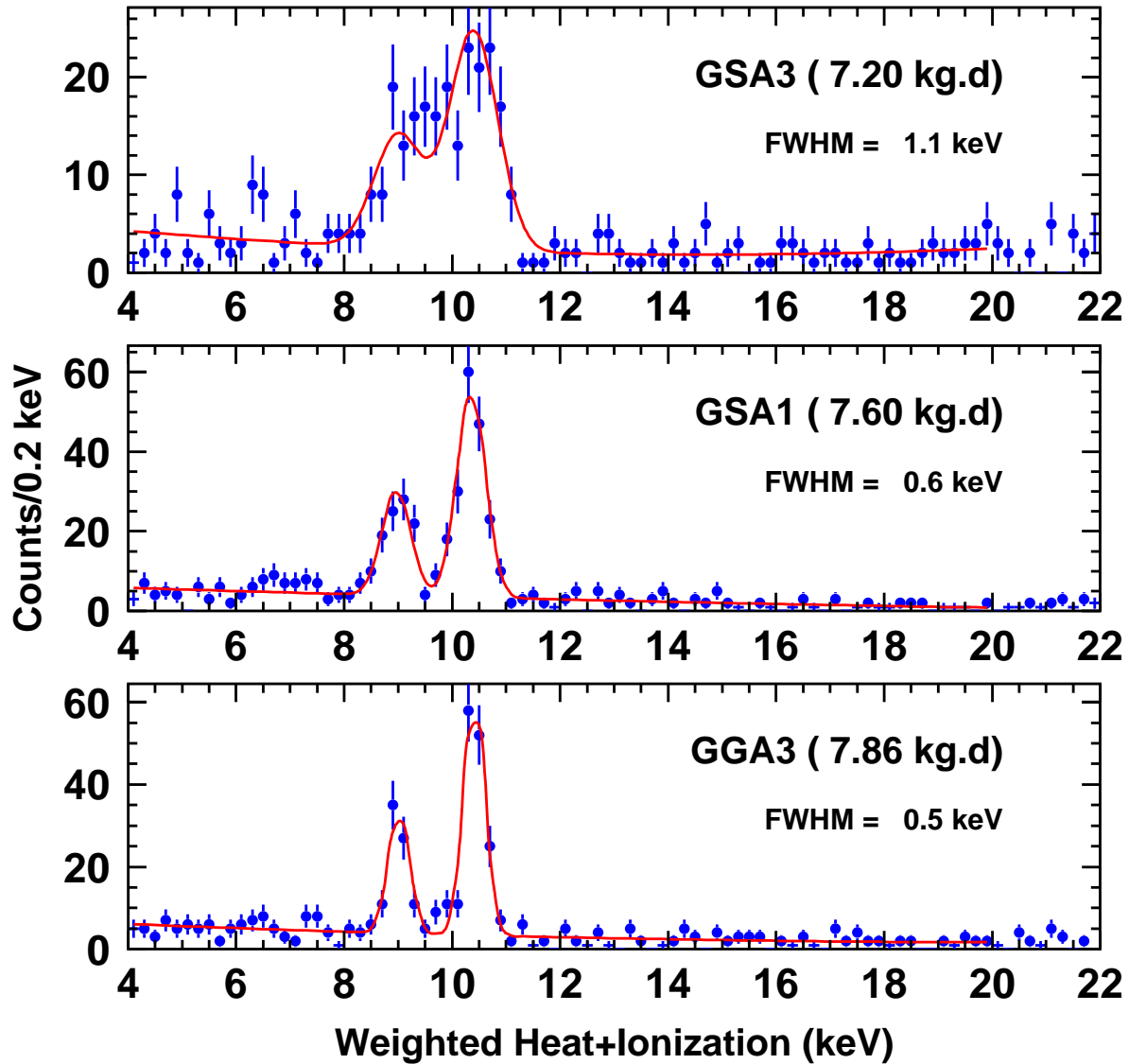


FIG. 2: Low-energy part of the spectrum recorded in the fiducial volume of the three detectors. The energy is calculated as the sum of the ionization and heat channels, weighted by their resolution squared. The peaks at 8.98 and 10.37 keV correspond to the de-excitation of the cosmogenic activation of  $^{65}\text{Zn}$  and  $^{68}\text{Ge}$  in the detectors, and the  $^{71}\text{Ge}$  activation that follows neutron calibrations. The lines correspond to a Gaussian fit with the indicated value of FWHM resolutions.

## EDELWEISS-I - neutron coincidence calibration

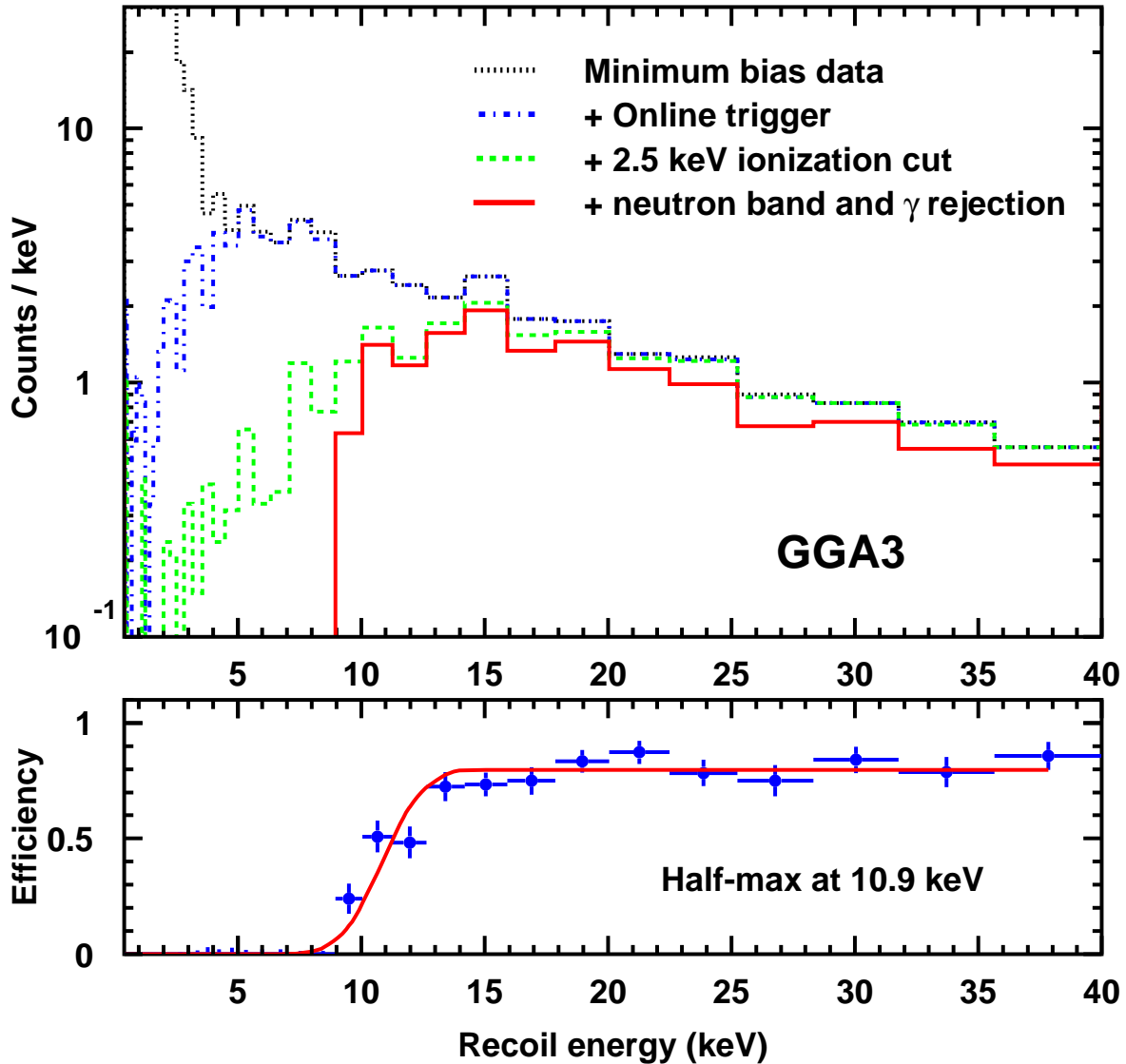


FIG. 3: Measurement of the efficiency as a function of recoil energy for the detector GGA3 in the run 2003p configuration, using neutron-coincidence data from a  $^{252}\text{Cf}$  calibration. Top: spectrum as a function of energy with different cuts. Dotted: minimum bias (selection based only on the presence of a neutron in the other two detectors); dot-dashed: adding the condition that the heat signal is above threshold; dashed: adding the 2.5 keV<sub>ee</sub> ionization cut; full line: adding the  $\pm 1.65\sigma$  and  $< -3.29\sigma$  nuclear and electron recoil requirements (see text). Bottom: resulting efficiency as a function of energy. The maximum value is not 90 % because the data are not corrected for the effect of neutron- $\gamma$  coincidences.

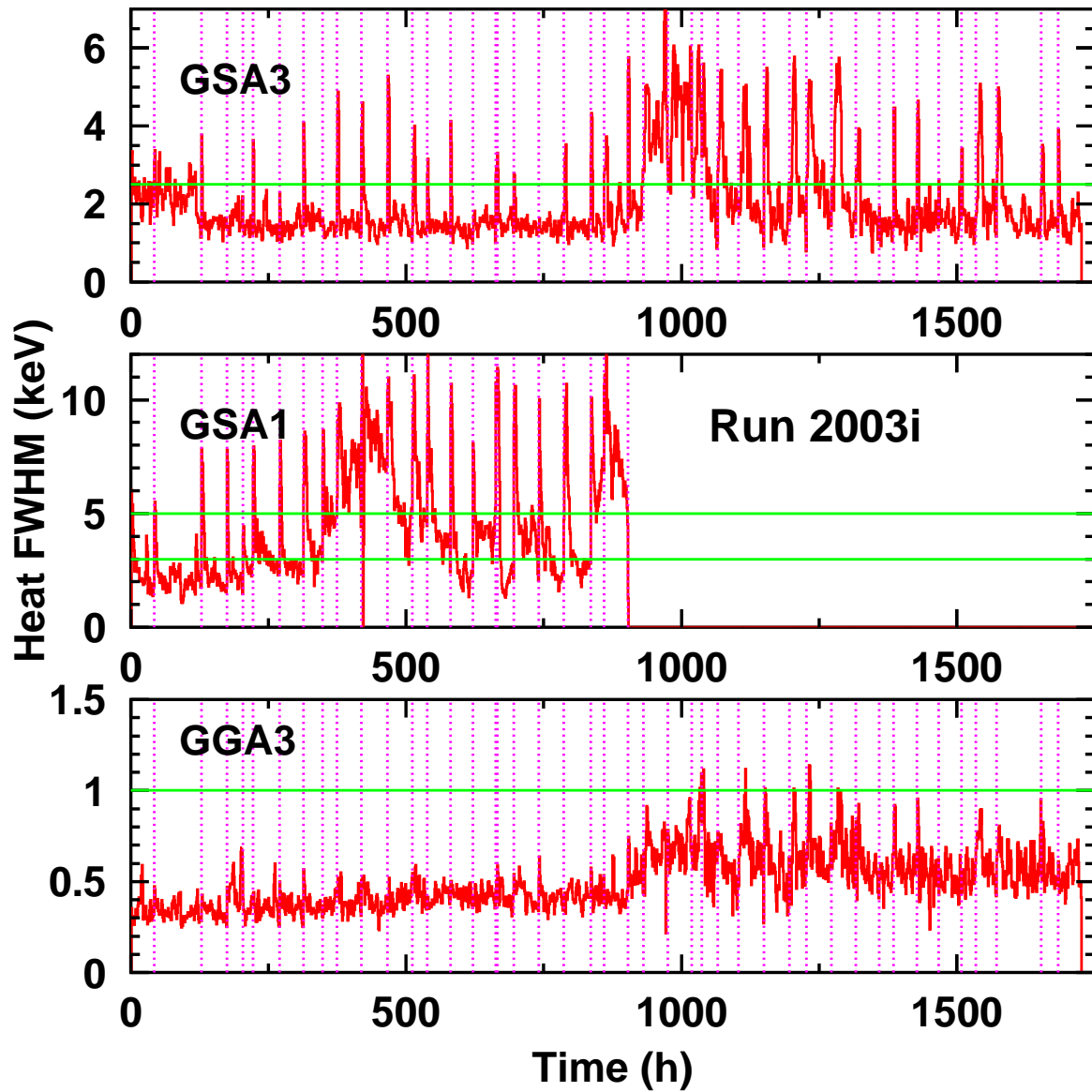


FIG. 4: Baseline FWHM resolution on the heat channel of the three detectors in the run 2003i as a function of time in hours since the beginning of the run. The resolution is evaluated by 3-hours intervals centered on each hour. The dotted lines represent times when the cryostat was re-filled with liquid He. The full lines represent FWHM cuts.

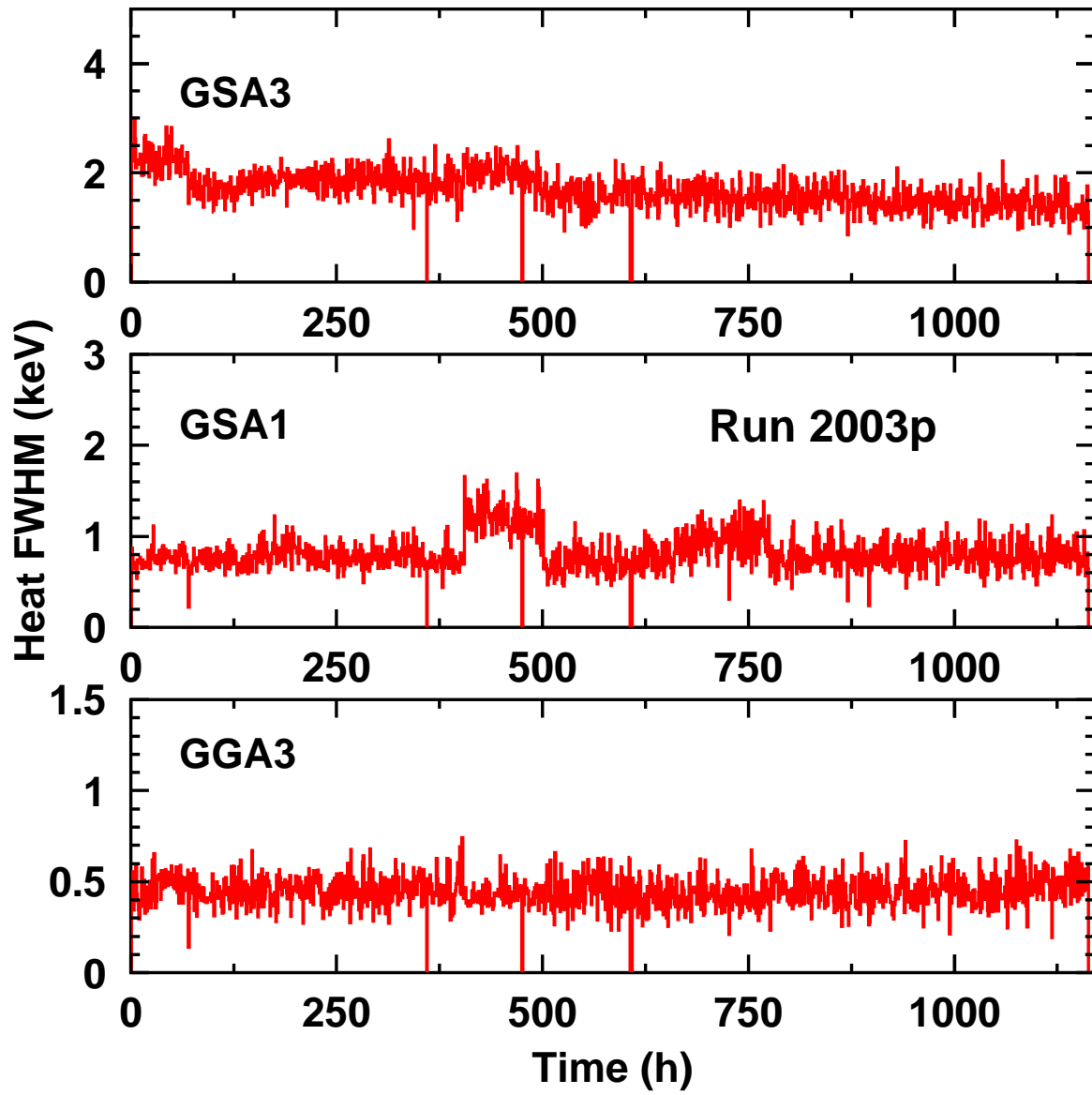


FIG. 5: Baseline FWHM resolution on the heat channel of the three detectors in the run 2003p as a function of time in hours since the beginning of the run. The resolution is evaluated by 3-hours intervals centered on each hour.



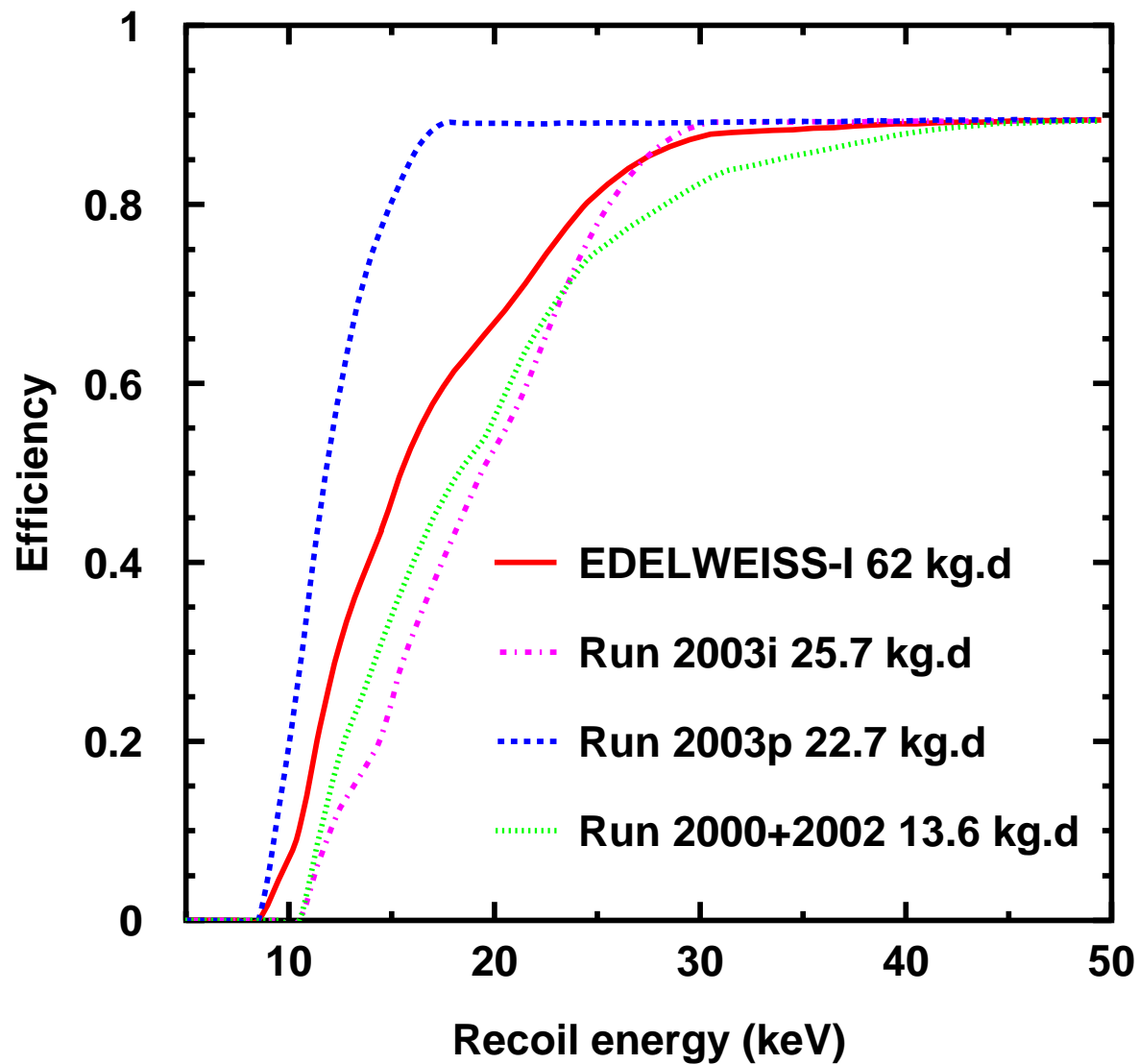


FIG. 6: Simulated efficiency, including all experimental cuts and resolutions, as a function of recoil energy, calculated for  $M_W = 100 \text{ GeV}/c^2$ , for runs 2000+2002, 2003i, 2003p and the sum of all EDELWEISS-I runs.

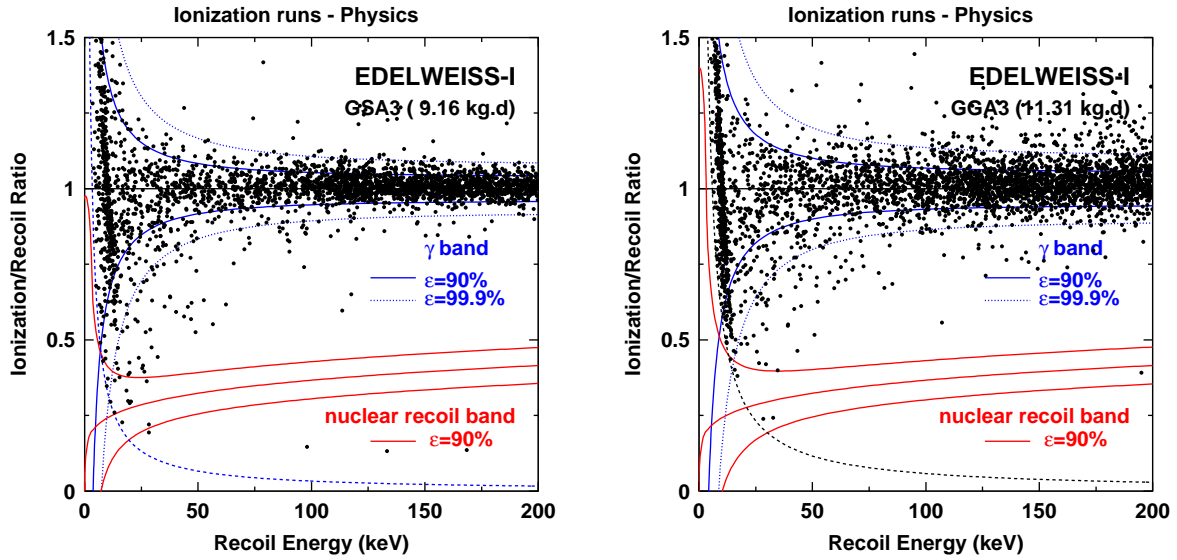


FIG. 7: Distribution of the quenching factor  $Q$  (ratio of the ionization to the recoil energies) as a function of the recoil energy  $E_R$  for data collected in the fiducial volume of GSA3 and GGA3 in the run 2003i. Also plotted as full lines are the  $\pm 1.65\sigma$  (90 %) electron and nuclear recoil bands. The dotted lines represent the  $\pm 3.29\sigma$  (99.9 %) electron recoil band. The hyperbolic dashed curve corresponds to the ionization energy threshold.

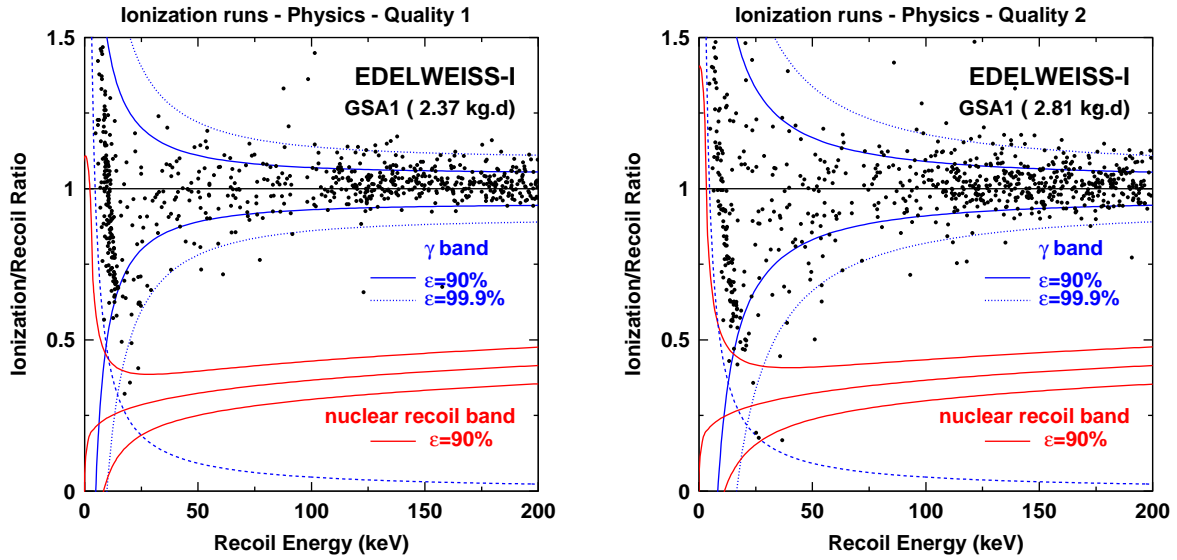


FIG. 8: Same as previous figure, for GSA1 in the run 2003i. Because of important fluctuations of the hourly average of the heat FWHM resolution, the data recorded with this detector are divided into two subsets according to whether this value is below  $3 \text{ keV}_{ee}$  (Quality 1) or between 3 and  $5 \text{ keV}_{ee}$  (Quality 2).

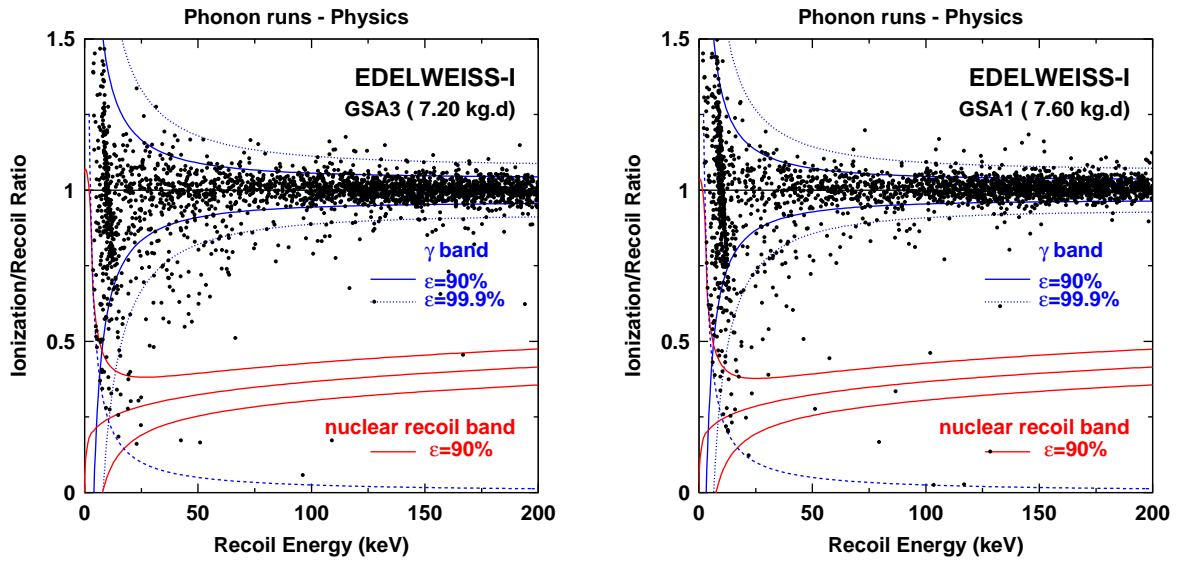


FIG. 9: Same as previous figure, for GSA3 and GSA1 in the run 2003p.

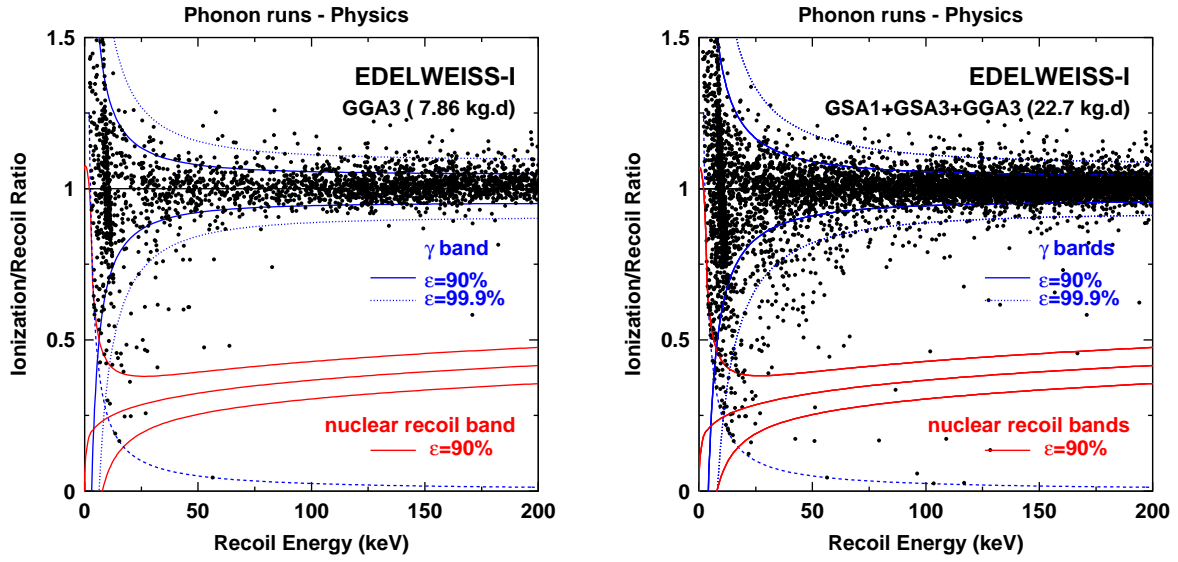


FIG. 10: Same as previous figure, for GGA3 and for the sum of the three detectors in the run 2003p.

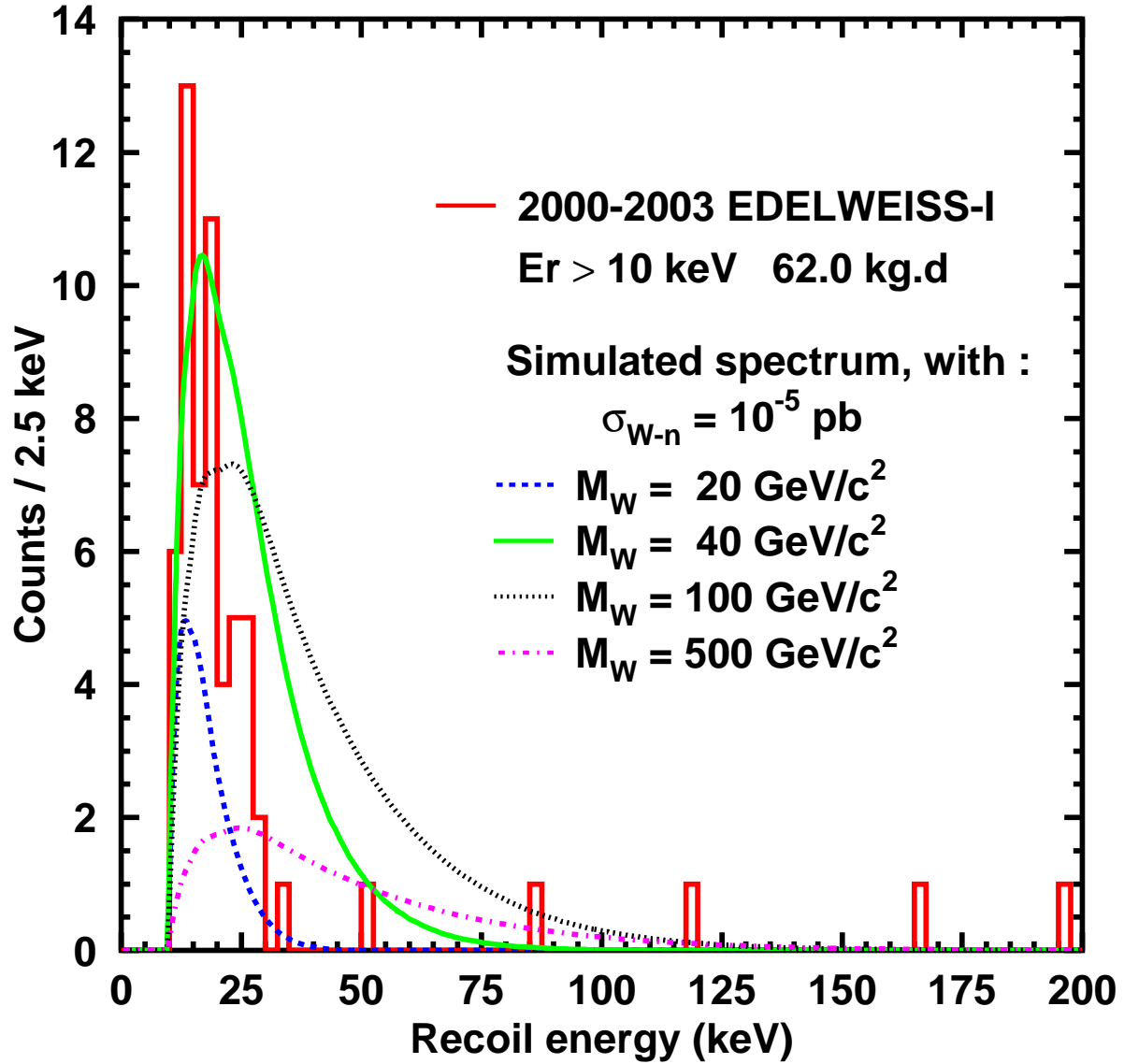


FIG. 11: Recoil energy spectrum of events in the nuclear recoil selection ( $E_R > 10 \text{ keV}$ ), recorded by EDELWEISS-I for a total fiducial exposure of 62 kg·d, compared with simulated WIMP spectra using a WIMP-nucleon scattering cross-section  $\sigma_{W-n} = 10^{-5} \text{ pb}$  for WIMP masses  $M_W = 20, 40, 100$  and  $500 \text{ GeV}/c^2$ .

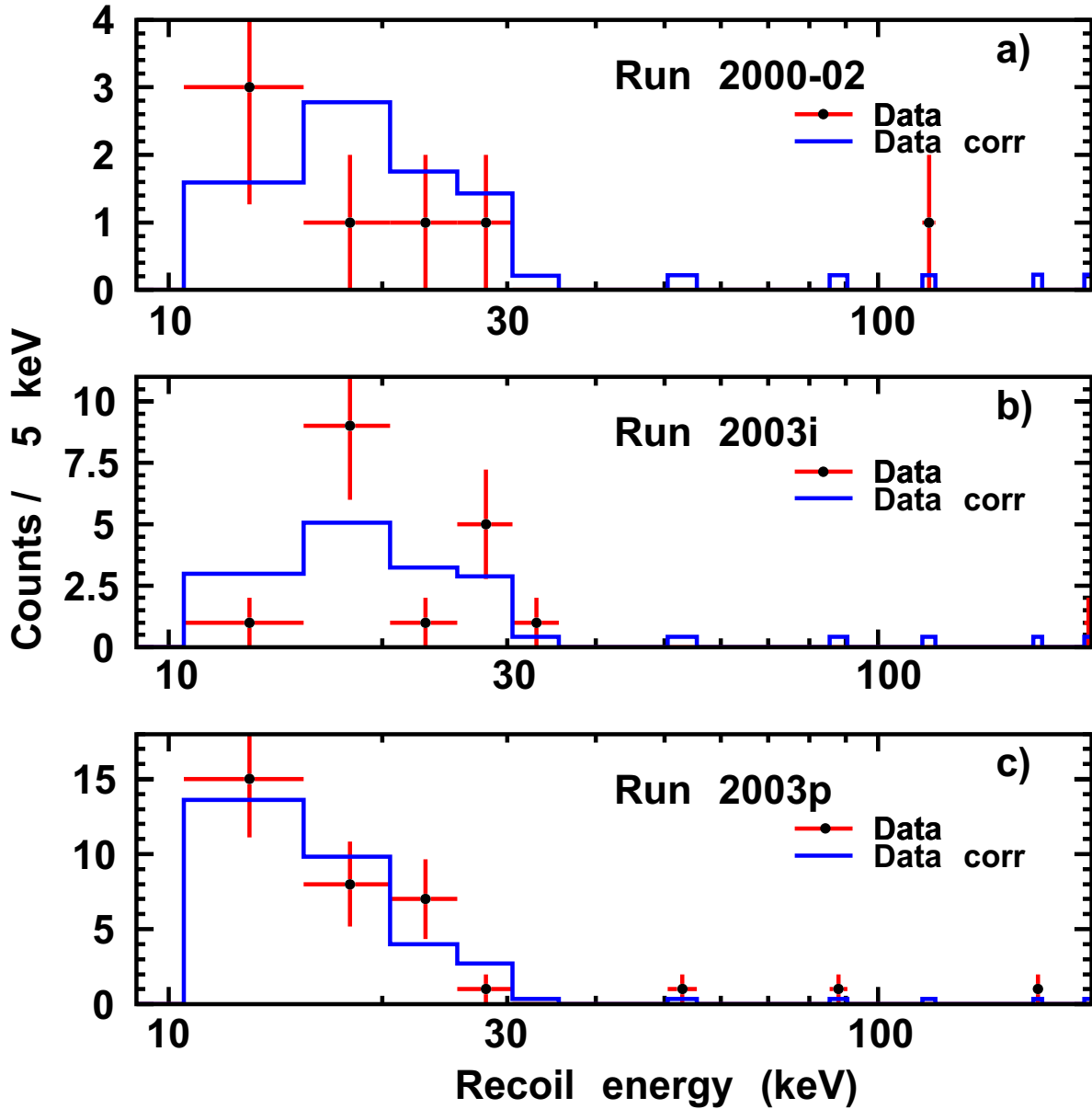


FIG. 12: Data points: recoil energy spectrum of events in the nuclear recoil selection recorded by EDELWEISS-I in the (a) 2000 and 2002, (b) 2003i and (c) 2003p runs. These spectra are compared with the efficiency-corrected average spectrum recorded in the entire data set (full-line histogram), obtained by multiplying the experimental spectrum of Fig. 11 by the ratio of energy-dependent efficiencies for the run of interest and for the entire data set.

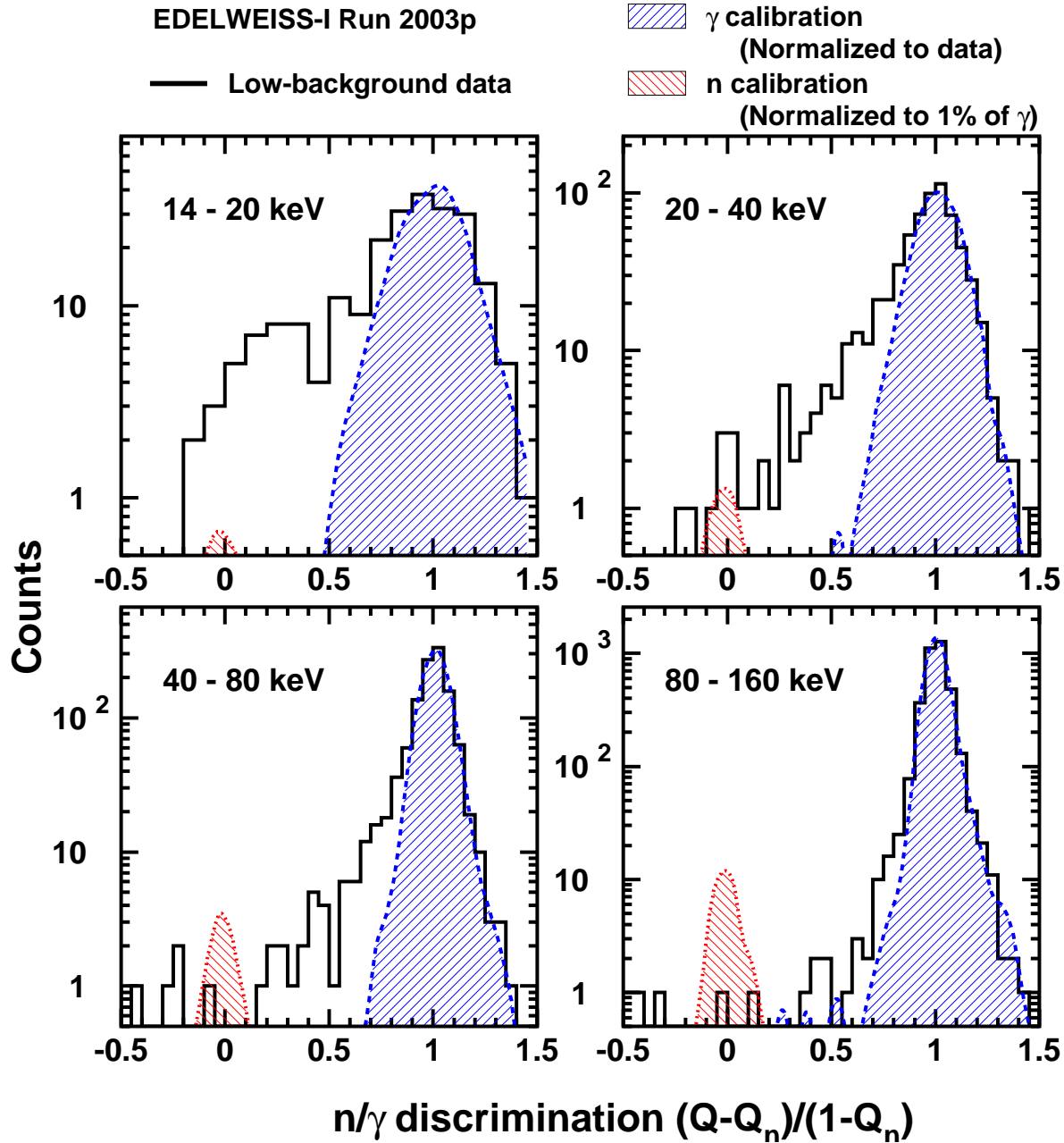


FIG. 13: Distribution of the normalized quenching  $D = (Q - Q_n)/(1 - Q_n)$  for four intervals of recoil energy (14-20, 20-40, 40-80 and 80-160 keV) for the three detectors in the run 2003p. With this variable, nuclear and electron recoils are centered at 0 and 1, respectively. Full line histogram: low-background run. Hatched distribution centered at 1: high-statistics  $\gamma$ -ray calibration ( $^{137}\text{Cs}$  source) normalized to the area of the upper half ( $Q > 1$ ) of the  $\gamma$ -ray peak in the low-background run. Hatched distribution centered at 0: high-statistics neutron source calibration ( $^{252}\text{Cf}$ ) normalized to 1 % of the area of the  $\gamma$ -ray peak.

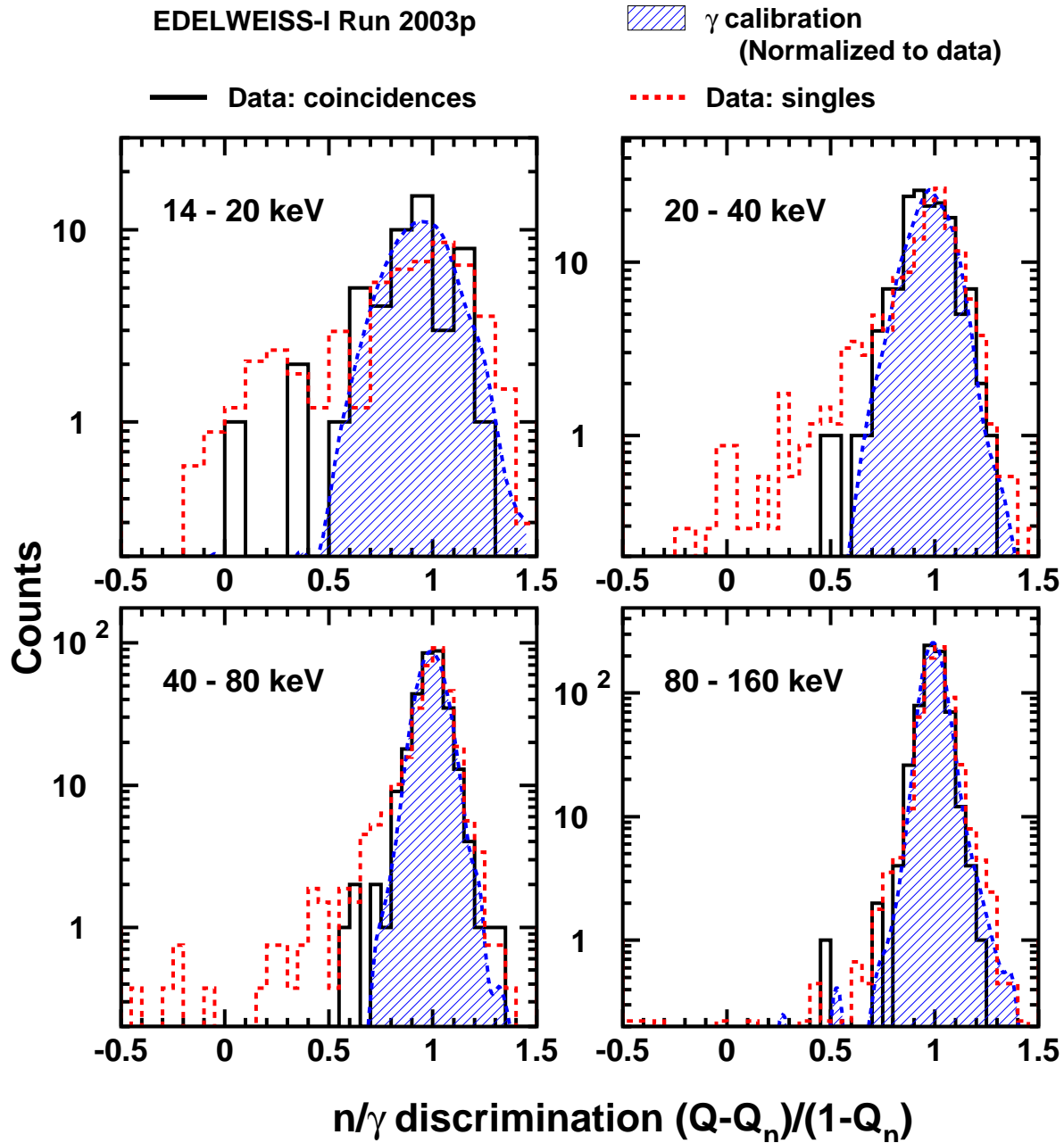


FIG. 14: Same as previous figure, except for coincidence (full line histogram) and single-detector (dashed line histogram) events. Hatched distribution: high-statistics  $\gamma$ -ray calibration ( $^{137}\text{Cs}$  source). All spectra are normalized to the area of the upper half ( $Q > 1$ ) of the  $\gamma$ -ray peak of the coincidences in the low-background run.



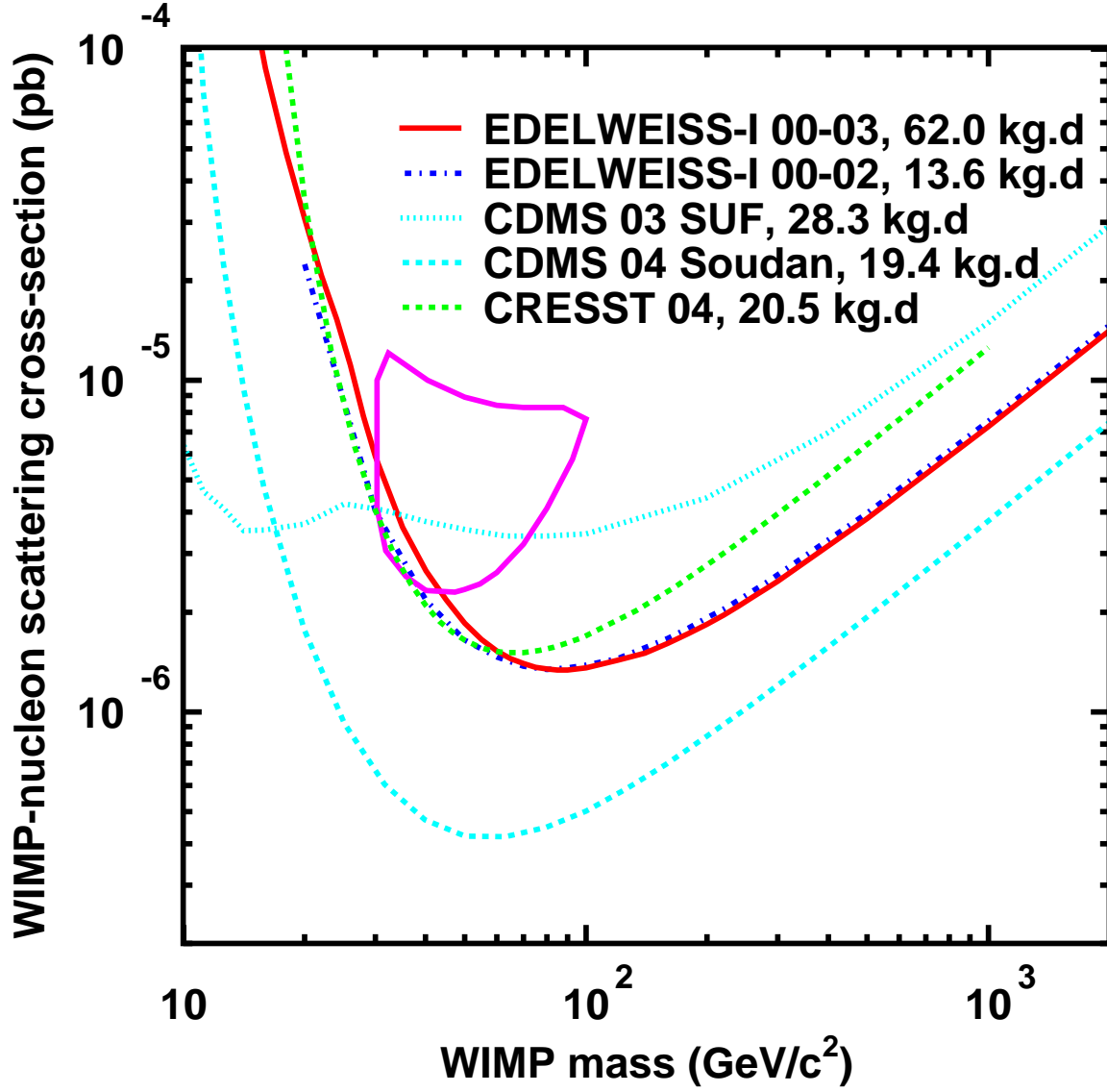


FIG. 15: 90 % C.L. spin independent limits (solid curve) obtained by EDELWEISS-I for a total fiducial exposure of 62 kg·d, for  $E_R > 15$  keV. Dotted curve : 2003 CDMS limits [5]. Light dashed curve : 2004 CDMS limits [6]. Dark dashed curve : CRESST limits using W recoils [9]. Dash-dotted curve : previous published EDELWEISS-I limits [8]. Closed contour : allowed region at  $3\sigma$  C.L. from the DAMA 1-4 annual modulation data [22].

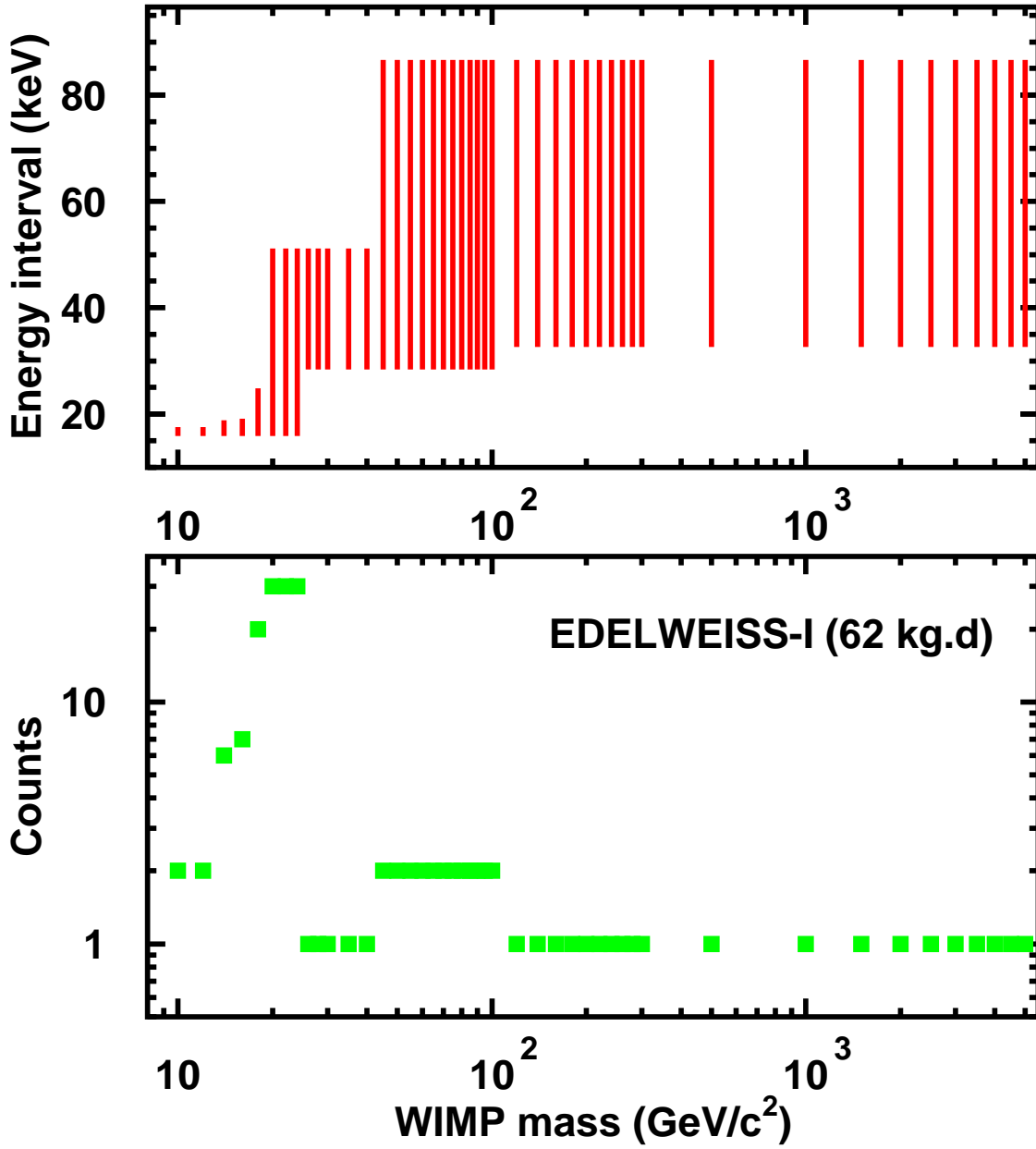


FIG. 16: Top: Recoil energy range selected by the Yellin algorithm used to derive the EDELWEISS-I 90 % C.L. limit from its 62 kg·d fiducial data set, as a function of WIMP mass. Bottom: Number of events observed in the corresponding recoil energy range.